

Attractor Memory for Long-Term Time Series Forecasting: A Chaos Perspective

Jiaxi Hu¹, Yuehong Hu¹, Wei Chen¹, Ming Jin², Shirui Pan³, Qingsong Wen⁴, and Yuxuan Liang^{1†}

¹Hong Kong University of Science and Technology (Guangzhou)

²Monash University

³Griffith University

⁴Squirrel AI

¹jiaxiu@hkust-gz.edu.cn, yuxliang@outlook.com

Abstract

In long-term time series forecasting (LTSF) tasks, an increasing number of models have acknowledged that discrete time series originate from continuous dynamic systems and have attempted to model their dynamical structures. Recognizing the chaotic nature of real-world data, our model, **Attraos**, incorporates chaos theory into LTSF, perceiving real-world time series as observations from unknown high-dimensional chaotic dynamic systems. Under the concept of attractor invariance, Attraos utilizes non-parametric Phase Space Reconstruction embedding and the proposed multi-scale dynamic memory unit to memorize historical dynamics structure and pblueicts by a frequency-enhanced local evolution strategy. Detailed theoretical analysis and abundant empirical evidence consistently show that Attraos outperforms various LTSF methods on mainstream LTSF datasets and chaotic datasets with only one-twelfth of the parameters compablue to PatchTST.

1 Introduction

In the intricate dance of time, time series unfold. Emerged from continuous dynamic systems [11, 32, 35], these series are meticulously collected at specific sampling frequencies. Like musical notes in a composition, they harmonize, revealing patterns that resonate through the symphony of temporal evolution. In this realm, Long-term Time Series Forecasting (LTSF) stands as one of the enduring focal points within the machine learning community, achieving widespread recognition in real-world applications, such as weather forecasting, financial risk assessment, and traffic prediction [20, 23, 24, 26].

Building on the success of various deep LTSF models [20, 25, 42, 43, 44, 46], which primarily leverage neural networks to learn temporal dependencies from discretely sampled data. Currently, researchers [28, 39] have been investigating the application of Koopman theory [41] in recovering continuous dynamic systems, which applies linear evolution operators to analyze dynamic system characteristics in a sufficiently high-dimensional Koopman function space. Nevertheless, the existence of Koopman space relies on the deterministic system, posing challenges given the chaotic nature of real-world time series data, evidenced through the Maximal Lyapunov Exponent in Appendix E.2.

In this paper, inspired by chaos theory [8], we revisit LSTF tasks from a chaos perspective: Linear or complex nonlinear dynamic systems exhibit stable patterns in their trajectories after sufficient evolution, known as attractors. As illustrated in Figure 1(a), attractors can be classified into four types: Fixed Point, indicating stable, invariant systems; Limited cycle, representing periodic behavior; Limited Toroidal, exhibiting quasi-periodic behavior with non-intersecting rings in a 2D plane, reflecting temporal distribution shifts; and Strange Attractor, characterized by nonlinear behavior and complex, non-topological shapes.

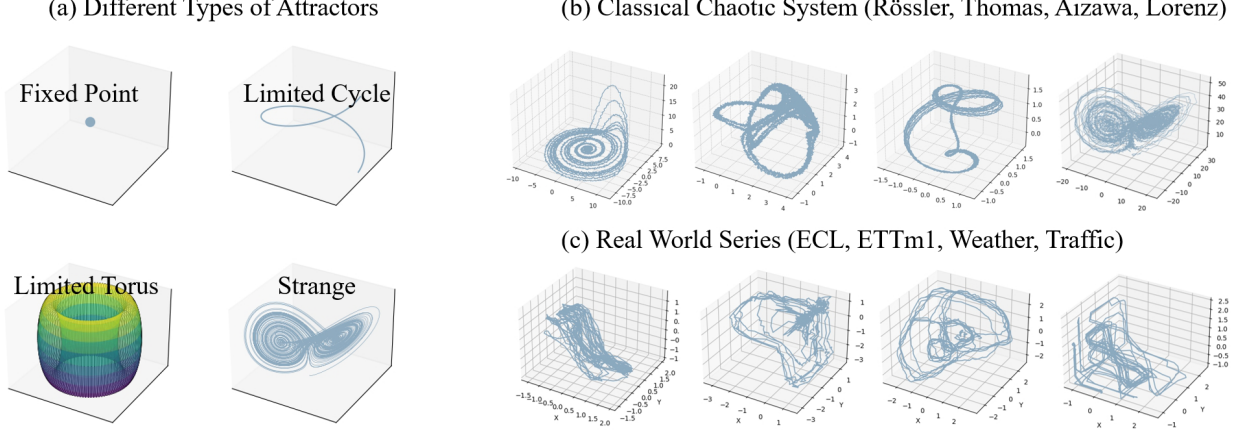


Figure 1: (a): Classical chaotic systems with noise. (b): Dynamic system structure of real-world datasets. (c): Different types of Attractors. See more figures in Appendix E.1.

Supported by chaos theory, we can transcend the limitations of deterministic dynamical systems to construct generalized dynamical system models. Figure 1(b-c) showcases various classical chaotic dynamic systems and the dynamic trajectories of real-world LTSF datasets using the phase space reconstruction method [9]. Notably, the dynamic system trajectories in these LTSF datasets exhibit fixed structures akin to those in typical chaotic systems.

Given this chaos perspective, we consider real-world time series as stemming from an unidentified high-dimensional underlying chaotic system, broadly encompassing nonlinear behaviors beyond periodicity. Our focus centers on recovering continuous chaotic dynamic systems from discretely sampled data for LTSF tasks, with the goal of predicting future time steps through the lens of attractor invariance. Specifically, this problem can be decomposed into two key questions: *(i) how to model the underlying continuous chaotic dynamic system based on discretely sampled time series data;* *(ii) how to enhance forecasting performance by utilizing the attractors within the system.*

In this context, **Attraos** comes into existence with the goal of capturing the underlying order within the seeming chaos via attractors. For tackling the first question, we employ a non-parametric phase space reconstruction method to recover the temporal dynamics and propose a *Multi-resolution Dynamic Memory Unit* (MDMU) to memorize the structural dynamics within historical sampled data. Specifically, as polynomials have been proven to be universal approximators for dynamic systems [4], MDMU expands upon the work of the State Space Model (SSM) [10, 12, 18] to different orthogonal polynomial subspaces. This allows for memorizing diverse dynamic structures that encompass various attractor patterns, while theoretically minimizing the boundary of attractor evolution error.

To address the second question, we devise a frequency-enhanced local evolution strategy, which is built upon the recognition that attractor differences are amplified in the frequency domain, as observed in the field of neuroscience [5, 6, 14]. Concretely, for dynamic system components that belong to the same attractor, we apply a consistent evolution operator to derive their future states in the frequency domain. Our contributions can be summarized as follows:

- **A Chaos Lens on LTSF.** We incorporate chaos theory into LTSF tasks by leveraging the concept of attractor invariance, leading to a principal way to model the underlying continuous dynamics
- **Efficient Dynamic Modeling.** Our model Attraos employs a non-parametric embedding to obtain high-dimensional dynamical representations, leverages MDMU to capture the multi-scale dynamical structure, and performs the evolution in the frequency domain. Remarkably, Attraos achieves this with only about one-twelfth the parameter count of PatchTST. Furthermore, we utilize the Blelloch scan algorithm [3] to enable efficient computation of the MDMU.
- **Empirical Evidence.** Various experiments validate the superior performance of Attraos. Besides Leveraging the properties of chaotic dynamic systems, we explore their extended applications in LTSF

tasks, focusing on chaotic evolution, modulation, representation, and reconstruction.

2 Preliminary

Attractor in Chaos Theory. In chaos theory, the interaction of three or more variables exhibiting periodic behavior gives rise to a complex dynamic system characterized by chaos. According to Takens’s theorem [30], assuming an ideal dynamic system $\mathcal{F} : \mathcal{M} \rightarrow \mathcal{M}$ that “lives” on attractor \mathcal{A} in manifold space \mathcal{M} which locally \mathcal{C}^N (N -times differentiable), time series data $\{z_i\} \in \mathbb{R}$ can be interpreted as the observation of it by an unknown observation function h . To explore the properties of the unknown ideal dynamic system, we can employ the phase space reconstruction (PSR) method to establish an approximation $\mathcal{K} : \mathbb{R}^m \rightarrow \mathbb{R}^m$ which lives in differential homomorphism attractor $\tilde{\mathcal{A}}$ in the Euclidean space with suitable dimension m [9]. The whole process is illustrated in Equation (1), where $\{z_i\}$, $\{u_i\}$ are the sampled data from two dynamic systems. Strictly speaking, in our paper, the chaotic attractor structure $\tilde{\mathcal{A}} = \{\tilde{\mathcal{A}}_i\}$ we focused on is in phase space \mathbb{R}^m . To facilitate understanding, we further provide a visual example of the Lorenz96 system in Appendix E.3.

In the forecasting stage, the local prediction method emerges as a prominent one: $u_{i+1} = \mathcal{K}^{(i)}(u_i)$, where the local evolution $\mathcal{K}^{(i)}$ can be either linear or nonlinear neural network [2, 36, 38], with the parameter being shared among the points in the neighborhood of u_i or belong to the same local attractor. Considering the universal approximation capabilities of polynomials for dynamic systems, we leverage the polynomial to describe the chaotic dynamic structures.

$$\begin{array}{ccc}
 a_i \in \mathcal{A} \subset \mathcal{M} & \xrightarrow{\mathcal{F}} & a_{i+1} \in \mathcal{A} \subset \mathcal{M} \\
 \downarrow h & & \downarrow h \\
 z_i \in \mathbb{R} & & z_{i+1} \in \mathbb{R} \\
 \downarrow \text{PSR} & & \downarrow \text{PSR} \\
 u_i \in \tilde{\mathcal{A}} \subset \mathbb{R}^m & \xrightarrow{\mathcal{K}} & u_{i+1} \in \tilde{\mathcal{A}} \subset \mathbb{R}^m
 \end{array} \quad (1)$$

$$x'(t) = \mathbf{A}x(t) + \mathbf{B}u(t) \quad (2a)$$

$$x(t) = (K * u)(t) \quad (2b)$$

$$K(t) = e^{t\mathbf{A}}\mathbf{B} \quad (2c)$$

Polynomial Projection with Measure Window. We only consider the first part of the SSM (2a), which is a parameterized map that transforms the input $u(t)$ into an N -dimensional latent space. According to Hippo [11], it is mathematically equivalent to: given an input $u(s)$, a set of orthogonal polynomial basis $\phi_n(t, s)$ that $\int_{-\infty}^t \phi_m(t, s)\phi_n(t, s)ds = \delta_{m,n}$, and an inner product probability measure $\mu(t, s)$. This enables us to project the input $u(s)$ onto the polynomial basis along time dimension (3), and we can combine $\phi_n(t, s)\omega(t, s)$ as a kernel $K_n(t, s)$ (4). When $\omega(t, s)$ is defined in a time window $\mathbb{I}[t, t + \theta]$, it represents approximating the input over each window θ .

$$\langle u, \phi_n \rangle_\mu = \int_{-\infty}^t u(s)\phi_n(t, s)\omega(t, s)ds \quad (3) \quad x_n(t) = \int u(s)K_n(t, s)\mathbb{I}(t, s)ds. \quad (4)$$

When the basis and measure are solely dependent on time t , it can be expressed in a convolution form (2b). In this paper, we will utilize this property to project the dynamic trajectories $\{u_n\}$ in phase space onto the polynomial spectral domain with kernel $e^{t\mathbf{A}}\mathbf{B}$ (2c) for characterization.

3 Theoretical Analysis & Methods

The overall structure of Attraos is depicted in Figure 2. In this section, we will comprehensively describe the components of Attraos, along with the utilization of efficient computational methods.

3.1 Phase Space Reconstruction

According to chaos theory, the initial step involves constructing a topologically equivalent dynamic structure through the PSR. The preferred embedding method is typically the Coordinate Delay Reconstruction [30], which does not rely on any prior knowledge of the underlying dynamic system. By utilizing the discrete sampled data $\{z_i\}$ and incorporating two hyperparameters, namely, embedding dimension m , time delay τ , a trajectory $\{u_i\}$ in phase space can be constructed by Equation 5.

$$u_i = (z_{i-(m-1)\tau}, z_{i-(m-2)\tau}, \dots, z_i) \quad (5) \quad \mathcal{K}_{patch} = \text{Unfold}(\mathcal{K}, p, p). \quad (6)$$

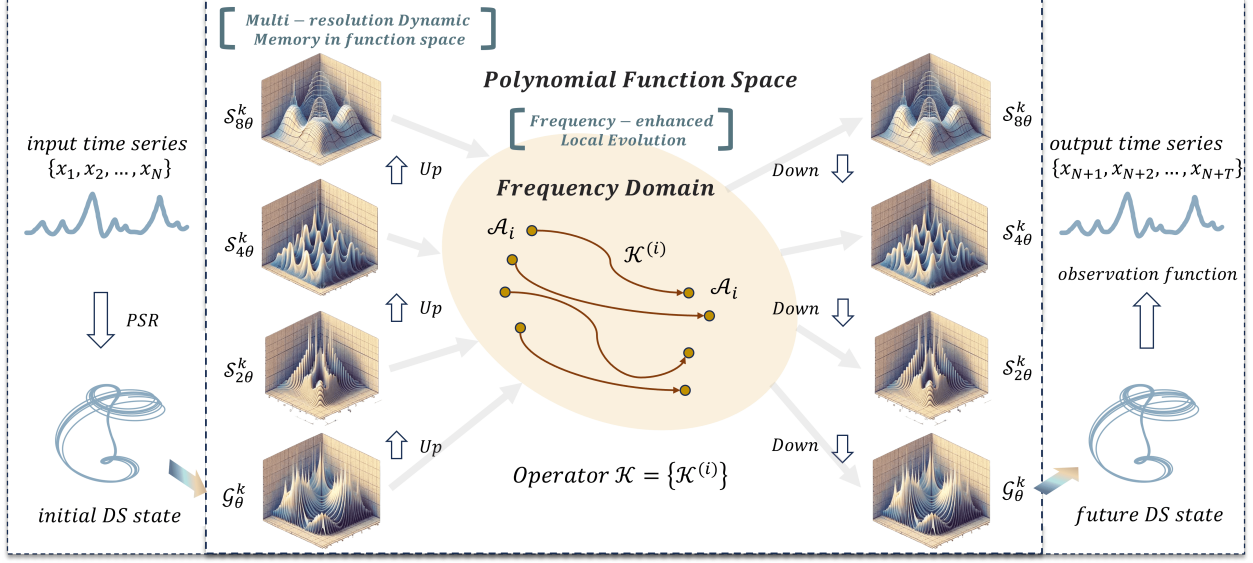


Figure 2: Overall architecture of Attraos. Initially, the PSR technique is employed to restore the underlying dynamic structures from historical data $\{z_i\}$. Subsequently, the dynamic system trajectory is fed into MDMU, projected onto polynomial space \mathcal{G}_{θ}^N using a time window θ and polynomial order N . Gradually, a hierarchical projection is performed to obtain more macroscopic memories of the dynamic system structure. Finally, local evolution operator $\mathcal{K}^{(i)}$ in the frequency domain is employed to obtain future state, thereby for the prediction.

For multivariate time series data with C variables, we have observed considerable variations in the Lyapunov exponents of each variable, hence a channel-independent strategy [29] is employed to construct a unified dynamic system $\mathcal{K} \subset \mathbb{R}^m$. To accelerate model convergence and reduce complexity, we apply non-overlapping patching to obtain \mathcal{K}_{patch} (6). We denote the number of patches as L , using $u \in \mathbb{R}^{B \times L \times D}$ to represent the tensor used for computing, where $D = mp$. The determination of m and τ is achieved by applying the CC method [21] as shown in Appendix C.1.

Remark 3.1. This represents the pioneering non-parametric embedding in LTSF, effectively reducing the model parameters in the embedding and output projection process (m is typically single-digit).

3.2 Dynamic Representation by MDMU

Proposition 1. $\mathbf{A} = \text{diag}\{-1, -1, \dots\}$ is a rough approximation of normal Hippo-LegT [11] matrix.

Remark 3.2. All proofs in this section can be found in Appendix B.

Adhere to Mamba [10], we generate \mathbf{B} and measure window θ by linear layer, and propose a novel parameterized method (Proposition 1) for \mathbf{A} to instantiate Equation 2a.

$$\mathbf{A} = \text{Broadcast}_D(\text{diag}\{-1, -1, \dots\}), \quad \mathbf{B} = \text{Linear}_{\mathbf{B}}(u), \quad \Delta/\theta = \text{softplus}(\text{Linear}_{\Delta}(u)). \quad (7)$$

where $\mathbf{A} \in \mathbb{R}^{D \times N}$ represents the dynamic characteristics of the system's forward evolution in the polynomial space. Due to its diagonal nature, its representational capacity is comparable to $\mathbb{R}^{D \times N \times N}$; Matrix $\mathbf{B} \in \mathbb{R}^{B \times L \times N}$ controls the process of projecting u onto the polynomial domain like a gate mechanism; The learnable approximation window $\Delta \in \mathbb{R}^{B \times L \times D}$, similar to an attention mechanism, enables adaptive focus on specific dynamic structures (attractors).

Remark 3.3. In the Hippo theory, the measure window is denoted by θ , while in SSMs [10, 12], the discrete step size is represented by Δ . These two terms can be considered approximately equivalent.

As shown in Figure 3(a), in practical computations, we need to discretize Equation 2a to fit the discrete dynamical trajectories. We apply zero-order hold (ZOH) discretization [11] to matrix \mathbf{A} , while opting for a

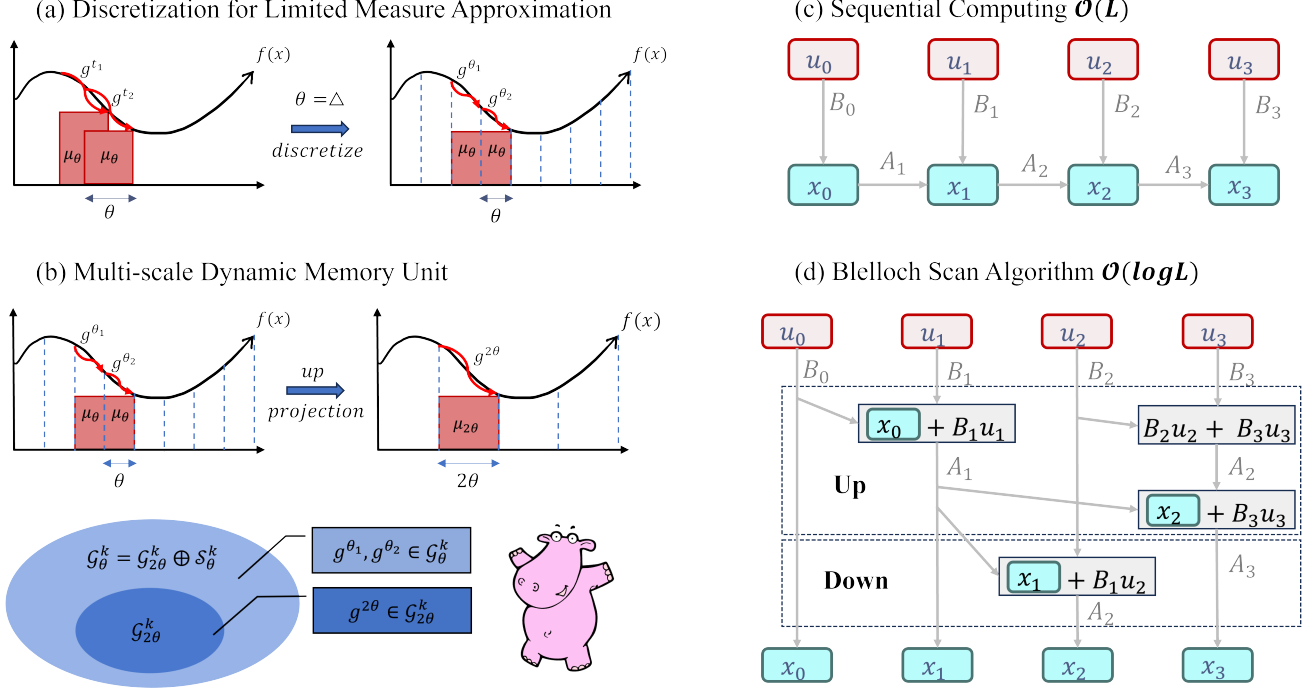


Figure 3: (a) Discretization of continuous polynomial approximation for sequence data. g represents the optimal polynomial constructed from polynomial bases. (b) MDMU projects the dynamical structure onto different orthogonal subspaces \mathcal{G} and \mathcal{S} . (c) Sequential computation for Equation 2a in $\mathcal{O}(L)$ time complexity. (d) Blelloch tree scanning for Equation 2a in $\mathcal{O}(\log L)$ by storing intermediate results.

combination of Forward Euler discretization for \mathbf{B} (instead of the commonly used $\overline{\mathbf{B}} = (\Delta\mathbf{A})^{-1}(\exp(\Delta\mathbf{A}) - \mathbf{I}) \cdot \Delta\mathbf{B}$ in SSMs), resulting in a more concise representation.

$$(\mathbf{ZOH}) : \overline{\mathbf{A}} = \exp(\Delta\mathbf{A}), \quad (\mathbf{Forward Euler}) : \overline{\mathbf{B}} = \Delta\mathbf{B}. \quad (8)$$

Next, we can project the dynamics trajectory u onto the polynomial domain using the discretized kernel to obtain dynamic representation $x \in \mathbb{R}^{B \times L \times D \times N}$ (9). This process can be achieved with $\mathcal{O}(L)$ complexity by employing sequential computation (Figure 3(c)) or by utilizing the Blelloch scan (Figure 3(d)) to store intermediate results with $\mathcal{O}(\log L)$ complexity.

$$\overline{\mathbf{K}} = \left(\overline{\mathbf{B}}, \overline{\mathbf{A}}\overline{\mathbf{B}}, \dots, \overline{\mathbf{A}}^{L-1}\overline{\mathbf{B}} \right), \quad x = u * \overline{\mathbf{K}}. \quad (9)$$

Up to this point, the construction of the underlying continuous dynamic system \mathcal{K} and its application to discretely sampled data z_n have been established. However, in this scenario, we are still limited to a single representation of the dynamic structures with measure window θ . The strange attractors, on the other hand, are often composed of multiple fundamental topological structures. Therefore, we require a multi-scale hierarchical representation of dynamic structures to capture their complexity.

To address this, as illustrated in Figure 3(b), we progressively increase the length of the window θ by powers of 2. The region previously approximated by $g^{\theta_1} \in \mathcal{G}_\theta^N$ (left half) and $g^{\theta_2} \in \mathcal{G}_\theta^N$ (right half) will now be approximated by $g^{2\theta} \in \mathcal{G}_{2\theta}^N$. Since $\mathcal{G}_{2\theta}$ is the subspace of \mathcal{G}_θ , the projection coefficients on these two spaces can be mutually transformed using the linear projection matrix H and its inverse matrix H^\dagger based on the odd or even positions along the L dimension in x .

$$x^{2\theta} = H^{\theta_1} x^{\theta_1} + H^{\theta_2} x^{\theta_2}, \quad x^{2\theta} \in \mathbb{R}^{B \times L/2 \times D \times N} \quad (10)$$

Remark 3.4. Although Δ is akin to a attention mechanism leads to different measure windows, ie., $\theta_1 \neq \theta_2$, it

still maintains the linear projection property for up and down projection: $\mathcal{G}_{\theta_1}, \mathcal{G}_{\theta_2} \leftrightarrow \mathcal{G}_{\theta_1+\theta_2}$. In our illustration, we have used a unified measure window for simplicity.

Iteratively repeating this process enables us to model the dynamic structure from a more macroscopic perspective. Theorem 2 indicates that under this approach, the polynomial projection error has convergence of order N . Hyper-parameter analysis can be found in the experiment section.

Remark 3.5. When the weight function is uniformly equal across the dynamic structure, H^{θ_1} and H^{θ_2} are shared in each projection level as the projection matrix for the left and right interval.

Theorem 2. (Approximation Error Bound) Function $f : [0, 1] \in \mathbb{R}$ is k times continuously differentiable, the piecewise polynomial $g \in \mathcal{G}_r^N$ approximates f with mean error bounded as:

$$\|f - g\| \leq 2^{-rN} \frac{2}{4^N N!} \sup_{x \in [0, 1]} |f^{(N)}(x)|.$$

Based on this hierarchical projection, we additionally want to uphold the constancy of attractor patterns throughout the evolution, which is equivalent to minimizing attractor evolution errors. According to Theorem 3, it is imperative to ensure the separation between attractors, denoted as $\nabla_i := \min_{j, j \neq i} (\tilde{A}_i^T \tilde{A}_j - \tilde{A}_i^T \tilde{A}_i)$, is sufficiently large. While there is an intersection between the \mathcal{G}_θ^N and $\mathcal{G}_{2\theta}^N$ spaces, which limits the attainment of a sufficiently large ∇ . To address this issue, we define an orthogonal complement space as $\mathcal{G}_\theta^N = \mathcal{S}_\theta^N \oplus \mathcal{G}_{2\theta}^N$, to establish a series of orthogonal function spaces $\{\mathcal{S}_\theta^N, \mathcal{S}_{2\theta}^N, \dots, \mathcal{S}_{2^L\theta}^N, \mathcal{G}_{2^L\theta}^N\}$. We can extend Equation 10 as: (Details in Appendix A.4)

$$x^{2\theta} = H^{\theta_1} x^{\theta_1} + H^{\theta_2} x^{\theta_2}, \quad s^{2\theta} = G^{\theta_1} x^{\theta_1} + G^{\theta_2} x^{\theta_2}, \quad (11)$$

$$x^{\theta_1} = H^{\dagger\theta_1} x^{2\theta} + G^{\dagger\theta_1} s_t^{2\theta}, \quad x^{\theta_2} = H^{\dagger\theta_2} x^{2\theta} + G^{\dagger\theta_2} s_t^{2\theta}. \quad (12)$$

Theorem 3. The mean **attractor evolution error** $\|\mathcal{K} \circ \tilde{A} - \tilde{A}\|$ of evolution operator $\mathcal{K} = \{\mathcal{K}^{(i)}\}$ is bounded by $\|\mathcal{K} \circ \tilde{A} - \tilde{A}\|(N-1)\mathcal{E}(-\beta\nabla_i + 1)$, with the number of random patterns $N \geq \sqrt{pc} \frac{d-1}{4}$ stored in the system by interaction paradigm \mathcal{E} in an ideal spherical retrieval paradigm.

Theorem 4 states that the coarsest-grained \mathcal{G} space, along with a series of orthogonal complement \mathcal{S} spaces, can approximate any given dynamic system structure with finite error bounds in Theorem 2.

Theorem 4. (Completeness in L^2 space) The orthonormal system $B_N = \{\phi_j : j = 1, \dots, N\} \cup \{\psi_j^{rl} : j = 1, \dots, N; r = 0, 1, 2, \dots; l = 0, \dots, 2^r - 1\}$ spans $L^2[0, 1]$.

Remark 3.6. $H, G, H^\dagger, G^\dagger \in \mathbb{R}^{N \times N}$ are obtained by applying Gaussian Quadrature to Legendre polynomials [13]. The gradients of these matrices are subsequently utilized for adaptive optimization.

The hierarchical projection can be implemented explicitly using iterative display or can be efficiently computed through an implicit implementation proposed in Section 3.3.

3.3 System Evolution by Attractors

Following chaos theory, we employ a local evolution method $x_{i+1} = \mathcal{K}^{(i)}(x_n)$ to forecast future state. Given dynamics representations s/x , the subsequent step involves partitioning the attractor and utilizing the operator \mathcal{K}^i belonging to A_i for system evolution. We present three evolution strategies:

- **Direct Evolution:** We employ each representation $x_t/s_t \in \mathbb{R}^{D \times N}$ as the feature to partition adjacent points in the dynamic system trajectory into the same attractor using the K-means method. Subsequently, we evolve these points using a local operator $\mathcal{K}^{(i)}$.

- **Frequency-enhanced Evolution:** Inspired by neuroscience [6], where attractor structures are amplified in the frequency domain, we first obtain the frequency domain representation of the dynamic structure through Fourier transformation. Considering the dominant modes as attractors, we employ $\mathcal{K}^{(i)}$ to drive the system’s evolution in the frequency domain.
- **Hopfield Evolution:** Hopfield networks [16] are designed specifically for attractor memory retrieval (see Appendix A.2). In our approach, we utilize a modern version [34] of the Hopfield network for the evolution of dynamic systems, employing cross-attention operations. We treat the trainable attractor library as the *Key* and *Value*, while different scales of dynamic structure representations $\{s^\theta, s^{2\theta}, \dots, s^{2^L\theta}, x^{2^L\theta}\}$ serve as the *Query*, enabling sequence-to-sequence evolution.

Our experimental results in Table 4 demonstrate that the frequency-enhanced evolution strategy outperforms others comprehensively, and we introduce two implementation approaches:

Explicit Evolution. Initially, the finest dynamic representation x^θ is obtained using $\overline{\mathbf{K}}$, and then expanded to multiple scales $s^\theta, s^{2\theta}, \dots, s^{2^L\theta}, x^{2^L\theta}$. By applying the Fourier Transform, we select M low-frequency components as the primary modes. Each mode undergoes linear evolution $\mathcal{K}^{(i)} = W_i \in \mathbb{C}^{N \times N}$, followed by back projection to the original scale.

Implicit Evolution. However, explicit evolution methods inevitably increase the time complexity. To address this issue, inspired by the Belloch algorithm and hierarchical projection, which both utilize tree-like structures, we propose an implicit evolution method.

A Belloch scan [3, 37] (Figure 3(d)) defines a binary operator $q_i \bullet q_j := (q_{j,a} \odot q_{i,a}, q_{j,a} \otimes q_{i,b} + q_{j,b})$ used to compute the linear recurrence $x_k = \overline{\mathbf{A}}x_{k-1} + \overline{\mathbf{B}}u_k$. We take $L = 4$ as an example.

Up sweep for even position	Down sweep for odd position
$r_2 = c_1 \bullet c_2 = (\overline{\mathbf{A}}, \overline{\mathbf{B}}u_1) \bullet (\overline{\mathbf{A}}, \overline{\mathbf{B}}u_2) = (\overline{\mathbf{A}}^2, \overline{\mathbf{A}}\overline{\mathbf{B}}u_1 + \overline{\mathbf{B}}u_2)$ $q_4 = c_3 \bullet c_4 = (\overline{\mathbf{A}}, \overline{\mathbf{B}}u_3) \bullet (\overline{\mathbf{A}}, \overline{\mathbf{B}}u_4) = (\overline{\mathbf{A}}^2, \overline{\mathbf{A}}\overline{\mathbf{B}}u_3 + \overline{\mathbf{B}}u_4)$ $r_4 = r_2 \bullet q_4 = (\overline{\mathbf{A}}^2, \overline{\mathbf{A}}\overline{\mathbf{B}}u_1 + \overline{\mathbf{B}}u_2) \bullet (\overline{\mathbf{A}}^2, \overline{\mathbf{A}}\overline{\mathbf{B}}u_3 + \overline{\mathbf{B}}u_4)$ $= (\overline{\mathbf{A}}^4, \overline{\mathbf{A}}^3\overline{\mathbf{B}}u_1 + \overline{\mathbf{A}}^2\overline{\mathbf{B}}u_2 + \overline{\mathbf{A}}\overline{\mathbf{B}}u_3 + \overline{\mathbf{B}}u_4).$	$r_1 = r_0 \bullet c_1 = (I, 0) \bullet (\overline{\mathbf{A}}, \overline{\mathbf{B}}u_1) = (\overline{\mathbf{A}}, \overline{\mathbf{B}}u_1)$ $r_3 = r_2 \bullet c_3 = (\overline{\mathbf{A}}^2, \overline{\mathbf{A}}\overline{\mathbf{B}}u_1 + \overline{\mathbf{B}}u_2) \bullet (\overline{\mathbf{A}}, \overline{\mathbf{B}}u_3)$ $= (\overline{\mathbf{A}}^3, \overline{\mathbf{A}}^2\overline{\mathbf{B}}u_1 + \overline{\mathbf{A}}\overline{\mathbf{B}}u_2 + \overline{\mathbf{B}}u_3)$ $x_1, x_2, x_3, x_4 = r_1[R], r_2[R], r_3[R], r_4[R].$

The process commences by computing the values of variable x at even positions through an upward sweep. Subsequently, these even position values are employed during a downward sweep to calculate the values at odd positions. The corresponding value of x resides in the right node of r . Thus, we can modify the binary operator as $q_i \bullet q_j := (q_{j,a} \odot q_{i,a}, H_i \otimes (q_{j,a} \otimes q_{i,b} + q_{j,b}))$, thereby implicitly integrating hierarchical projection into the scanning operation. This leads to the scales of x_i is:

$$scale(x_i) = \begin{cases} 0 & \text{if } i = 0 \\ scale(x_{i-1}) + 1 & \text{if } i \text{ is odd} \\ \log_2(i) & \text{if } i \text{ is even and a power of 2} \\ 1 & \text{if } i \text{ is even and not a power of 2} \end{cases}$$

We simplify the original $\mathbf{H}^{\theta_1/\theta_2}, \mathbf{G}^{\theta_1/\theta_2}, \mathbf{H}^{\dagger\theta_1/\theta_2}, \mathbf{G}^{\dagger\theta_1/\theta_2}$ with just $\mathbf{H} \in \mathbb{R}^{B \times L \times N}$, which is generated directly through a linear layer, and omit the reconstruction process. This approach directly sparsifies the kernels $e^{\mathbf{A}^t \mathbf{B}}$ in different subspaces and using the linear layer to generate hierarchical space projection matrix. Afterwards, we learn the evolution using the data x in the frequency domain.

$$\mathbf{H} = \text{Linear}_{\mathbf{H}}(u), \quad \mathbf{W}_{out} = \text{Linear}_{\mathbf{W}_{out}}(u). \quad (13)$$

In Attraos, we utilize this indirect and efficient hierarchical projection as the default setting. Ultimately, Attraos projects from the polynomial spectral space back to the phase space by employing another gating projection $\mathbf{W}_{out} \in \mathbb{R}^{B \times L \times N \times 1}$ (13) to $x \in \mathbb{R}^{B \times L \times D \times N}$, and derives the prediction results using an observation function parameterized by $\mathbf{W}_h \in \mathbb{R}^{LD \times H}$ (flattening the patches).

Table 1: Average results of long-term forecasting with an input length of 96 and prediction horizons of {96, 192, 336, 720}. The best performance is in **Red**, and the second best is in **Blue**. Full results are in Appendix E.7.

Model	Attraos (Ours)		Mamba4TS		S-Mamba [40]		RWKV-TS [17]		GPT-TS [17]		Koopas [28]		InvTrm [27]		PatchTST [29]		DLinear [44]	
Metric	MSE	MAE	MSE	MAE	MSE	MAE	MSE	MAE	MSE	MAE	MSE	MAE	MSE	MAE	MSE	MAE	MSE	MAE
ETTh1	0.423	0.420	0.444	0.438	0.459	0.453	0.454	0.446	0.457	0.450	0.450	0.443	0.463	0.454	0.434	0.435	0.462	0.458
ETTh2	0.372	0.399	0.386	0.410	0.381	0.407	0.375	0.402	0.389	0.414	0.397	0.417	0.383	0.407	0.380	0.406	0.564	0.520
ETTm1	0.382	0.391	0.396	0.406	0.399	0.407	0.391	0.403	0.396	0.401	0.395	0.403	0.407	0.412	0.403	0.398	0.403	0.406
ETTm2	0.280	0.324	0.299	0.343	0.289	0.333	0.285	0.330	0.294	0.339	0.281	0.326	0.291	0.335	0.283	0.329	0.345	0.396
Exchange	0.349	0.395	0.364	0.405	0.364	0.407	0.406	0.439	0.371	0.409	0.390	0.424	0.366	0.416	0.383	0.416	0.346	0.416
Crypto	0.187	0.157	0.193	0.162	0.198	0.163	0.190	0.159	0.196	0.164	0.199	0.165	0.196	0.164	0.192	0.161	0.201	0.176
Weather	0.246	0.271	0.258	0.280	0.252	0.277	0.256	0.280	0.279	0.279	0.247	0.273	0.260	0.280	0.258	0.280	0.267	0.319

Table 2: Prediction results on the artificial (Lorenz96-3d) and real-world chaotic datasets (Air-convection) with various forecasting lengths. **Red/Blue** denotes the best/second performance.

Model		Attraos (Ours)		Mamba4TS (Temporal Emb.)		S-Mamba [40]		RWKV-TS [17]		Koopas [28]		InvTrm [27]		PatchTST [29]		DLinear [44]	
Metric		MSE	MAE	MSE	MAE	MSE	MAE	MSE	MAE	MSE	MAE	MSE	MAE	MSE	MAE	MSE	MAE
Lorenz96-3d	96	0.844	0.684	0.892	0.721	0.925	0.744	0.894	0.722	0.891	0.736	0.963	0.786	0.929	0.756	0.881	0.750
	192	0.835	0.662	0.910	0.748	0.917	0.761	0.894	0.744	0.881	0.752	0.944	0.811	0.899	0.714	0.910	0.753
	336	0.837	0.681	0.943	0.772	0.968	0.788	0.982	0.823	0.914	0.753	0.997	0.841	0.922	0.787	0.893	0.737
	720	0.872	0.739	0.996	0.814	1.135	0.940	1.058	0.921	0.989	0.801	1.129	0.955	0.971	0.828	0.927	0.806
	AVG	0.847	0.692	0.935	0.764	0.986	0.808	0.957	0.803	0.919	0.761	1.008	0.848	0.930	0.771	0.903	0.762
Air	96	0.437	0.303	0.451	0.314	0.468	0.329	0.447	0.308	0.443	0.307	0.470	0.337	0.465	0.331	0.441	0.325
	192	0.455	0.321	0.472	0.331	0.481	0.340	0.467	0.328	0.451	0.329	0.485	0.349	0.477	0.341	0.460	0.338
	336	0.456	0.334	0.468	0.342	0.485	0.351	0.461	0.339	0.468	0.342	0.499	0.363	0.484	0.353	0.461	0.341
	720	0.466	0.355	0.492	0.379	0.501	0.386	0.482	0.367	0.488	0.369	0.516	0.401	0.504	0.392	0.474	0.359
	AVG	0.454	0.328	0.471	0.342	0.484	0.352	0.464	0.336	0.463	0.337	0.493	0.363	0.483	0.354	0.459	0.341

4 Experiments

In this section, we commence by conducting a comprehensive performance comparison of Attraos against other state-of-the-art models in seven mainstream LTSF datasets along with two typical chaotic datasets, namely Lorenz96-3d and Air-Convection, followed by ablation experiments pertaining to model architectures. Furthermore, leveraging the properties of chaotic dynamic systems, we explore their extended applications, including experiments on chaotic evolution, representation, modulation, and reconstruction (the latter three are in Appendix E). Finally we provide the complexity analysis and robustness analysis. For detailed information regarding baseline models, dataset descriptions, experimental settings, hyper-parameter analysis, please refer to Appendix D.

4.1 Overall Performance

Mainstream LTSF Datasets. As depicted in Table 1, we can observe that: (a) Attraos consistently exhibits the best performance, closely followed by RWKV-TS and Koopa, which underscores the crucial role of modeling temporal dynamics in LTSF tasks. (b) The models based on state space models (Mamba4TS, S-Mamba) generally outperform the Transformer-based models (PatchTST, InvTrm), indicating the potential superiority of state space models as fundamental frameworks for temporal modeling. (c) Performance of the GPT-TS model, which relies on a pretrained large language model, is relatively average, suggesting the inherent challenge in directly capturing the dynamics of temporal data using such models. A promising avenue for future research lies in training a comprehensive foundational temporal dynamics model on a large scale or leverage pre-training to obtain an attractor tokenizer that is better suited for inputs to the large language model.

Chaotic Datasets. Table 2 presents the results on both artificial and real-world chaotic datasets. It can be observed that: (a) Attraos exhibits superior performance on both datasets, thanks to the utilization of the

Table 3: Results of ablation study. “w/o” denotes without. PSR: Phase Space Reconstruction; MS: Multi-scale hierarchical projection; TV: Time-varying \mathbf{B} and \mathbf{W}_{out} ; SPA: Specially initialized \mathbf{A} ; FE: Frequency Evolution. Red/Blue denotes the performance improvement/decline.

Model		Attraos		w/o PSR		w/o MS		w/o TV		w/o SPA		w/o FE	
Metric		MSE	MAE	MSE	MAE	MSE	MAE	MSE	MAE	MSE	MAE	MSE	MAE
ETTh2	96	0.292	0.348	0.301	0.357	0.299	0.353	0.299	0.354	0.294	0.351	0.297	0.352
	192	0.374	0.386	0.389	0.405	0.384	0.393	0.381	0.395	0.373	0.384	0.378	0.388
	336	0.420	0.432	0.427	0.438	0.426	0.436	0.424	0.430	0.425	0.436	0.427	0.435
	720	0.418	0.431	0.431	0.450	0.425	0.437	0.416	0.427	0.421	0.433	0.427	0.437
	AVG	0.376	0.399	0.387	0.413	0.380	0.405	0.380	0.402	0.478	0.401	0.382	0.403
Weather	96	0.159	0.206	0.171	0.215	0.163	0.210	0.167	0.214	0.162	0.209	0.164	0.211
	192	0.212	0.249	0.266	0.263	0.218	0.253	0.222	0.270	0.215	0.249	0.216	0.253
	336	0.265	0.288	0.282	0.304	0.271	0.295	0.277	0.297	0.263	0.288	0.270	0.294
	720	0.347	0.340	0.358	0.351	0.346	0.338	0.355	0.346	0.347	0.342	0.355	0.356
	AVG	0.246	0.271	0.259	0.283	0.250	0.274	0.255	0.282	0.247	0.272	0.251	0.279

PSR and MDMU modules, which effectively capture the multi-scale attractor structures. (b) In Lorenz96 dataset, where there is a prior knowledge about the phase space dimension, Attraos outperforms other models by a significant margin. This highlights the importance of PSR in recovering the complete temporal dynamics. (c) Apart from Attraos, the linear model (DLinear) demonstrate the best predictive results due to their robustness. Conversely, deep learning models based on transformers exhibit weaker performance and fail to model chaotic dynamics effectively.

4.2 Further Analysis

Ablation Studies. Next, we turn off each module of Attraos to assess their individual effects. As shown in Table 3, we observe consistent performance decline of Attraos when deleting each module: (a) The removal of Phase Space Reconstruction exhibits the most severe performance degradation, indicating that the process of reconstructing the dynamical structure through PSR forms the foundation for Attraos’ efficient capture of attractor structures. (b) Multi-scale hierarchical projection effectively captures the complex topological structure of the singular attractor, leading to improved performance. However, overfitting may occur in certain prediction lengths. (c) Time-varying \mathbf{B} and \mathbf{W}_{out} acts as a gating attention mechanism, allowing for a more focused emphasis on dynamic structural segments that potentially contain attractor structures, thereby enhancing performance. (d) The initialization method proposed for \mathbf{A} matrix demonstrates marginal yet consistent improvements, underscoring the importance of prior inductive bias for machine learning models. (e) Frequency domain evolution methods significantly reduce temporal noise information and amplify attractor structures. We will further analyze the importance of frequency domain evolution in subsequent analysis.

Chaotic Evolution Strategy. We further compare various dynamic system evolution strategies mentioned in Section 3.3. From Table 4, it is evident that the frequency-enhanced evolution strategy outperforms the others. Moreover, our proposed efficient implicit evolution method can adaptively explore multi-scale dynamical structure information, avoiding redundant cyclic computations and mitigating overfitting. (b) An inherent characteristic of time series data is significant noise, making it challenging to capture the underlying dynamical structures in the time domain. Direct evolution strategies, whether linear or non-linear neural network-based, do not yield satisfactory results. Moreover, according to the theorem 2 in FiLM [45], the recursion computation for dynamic projection further accumulates noise information. (c) Applying Hopfield networks in the time domain also proves to be unsatisfactory, and even adding more patterns (*Key* and *Value*) can have adverse effects. A potential solution is to apply Hopfield networks in the frequency domain instead.

Robustness Analysis. We add a $0.1 * \mathcal{N}(0, 1)$ Gaussian noise to the training dataset to test the robustness of Attraos. As shown in Table 5, it can be observed that Attraos exhibits strong robustness against noisy data, and increasing the level of noise can even lead to further performance improvement. This is attributed to the frequency domain evolution strategy, where we retain only the dominant modes as attractor structures, effectively removing the noise information. Furthermore, an interesting phenomenon has been observed in our experiments: as noise is introduced, the model’s convergence speed increases. This discovery warrants

Table 4: Results of various chaotic evolution strategies. Red/Blue denotes the best/second performance.

SSMs		Implicit Fre		Explicit Fre		Direct-Linear		Direct-CNN		Hopfield-16modes		Hopfield-64modes	
Metric		MSE	MAE	MSE	MAE	MSE	MAE	MSE	MAE	MSE	MAE	MSE	MAE
ETT _{h1}	96	0.370	0.388	0.376	0.392	0.388	0.404	0.395	0.410	0.384	0.405	0.389	0.407
	192	0.416	0.418	0.419	0.423	0.441	0.439	0.444	0.437	0.430	0.446	0.427	0.442
	336	0.458	0.432	0.465	0.439	0.488	0.460	0.482	0.456	0.480	0.482	0.485	0.489
	720	0.447	0.442	0.454	0.448	0.511	0.508	0.510	0.512	0.494	0.491	0.502	0.500
	AVG	0.423	0.420	0.429	0.426	0.457	0.453	0.458	0.454	0.447	0.456	0.426	0.460
ETT _{m2}	96	0.172	0.254	0.175	0.258	0.187	0.266	0.191	0.269	0.181	0.260	0.182	0.263
	192	0.242	0.301	0.247	0.308	0.264	0.331	0.265	0.334	0.255	0.312	0.259	0.314
	336	0.303	0.340	0.310	0.349	0.325	0.359	0.319	0.354	0.315	0.347	0.312	0.344
	720	0.401	0.399	0.407	0.405	0.424	0.419	0.421	0.422	0.420	0.426	0.417	0.422
	AVG	0.280	0.324	0.285	0.330	0.300	0.344	0.297	0.345	0.293	0.336	0.293	0.336

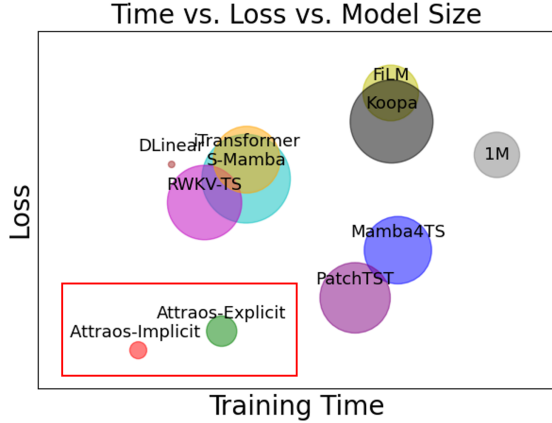


Figure 4: Complexity analysis.

Model		Attraos		Attrao-noise	
Metric		MSE	MAE	MSE	MAE
ETT _{h1}	96	0.370	0.388	0.360	0.390
	192	0.416	0.418	0.413	0.415
	336	0.458	0.432	0.455	0.430
	720	0.447	0.442	0.451	0.444
	AVG	0.423	0.420	0.422	0.420
ETT _{m2}	96	0.172	0.254	0.170	0.251
	192	0.242	0.301	0.238	0.297
	336	0.303	0.340	0.305	0.339
	720	0.401	0.399	0.398	0.392
	AVG	0.280	0.324	0.278	0.320

Table 5: Robustness analysis with additional noise. Red/Blue denotes the performance improvement/decline.

further exploration in future studies.

Complexity Analysis. As depicted in Figure 4, we present a comprehensive visual analysis comparing Attraos with various baseline models in terms of their average performance on the ETT_{h1} dataset. The x-axis represents the training time, the y-axis represents the test loss, and the circle radius corresponds to the model parameters. In this analysis, we substituted GPT-TS with FiLM due to its limited relevance to this specific evaluation. The results clearly demonstrate that Attraos surpasses other models in both time and space complexity, maintaining a significant advantage. Notably, when compared to the PatchTST model with a hidden dimension of 256 (2.4M parameters), Attraos (0.2M parameters) possesses only one-twelfth of its parameter count.

5 Conclusion and Future Work

LTSF tasks have long been a focal point of research in the machine-learning community. However, mainstream deep learning models currently overlook the crucial aspect that time series data is derived from discretely sampling underlying continuous dynamic systems. Inspired by chaotic theory, our model, Attraos, considers time series as generated by a generalized chaotic dynamic system. By leveraging the invariance of attractors, Attraos enhances predictive performance and provides empirical and theoretical explanations. We aim for Attraos to offer the machine-learning community a fresh perspective and inspire further research on the essence of time series dynamics.

There are still several unresolved issues that require further exploration. For instance: (a) PSR techniques exhibit sensitivity to the numerical values of time series data, and even for the same dataset, different embedding hyperparameters can be obtained. To address this, one potential solution is to utilize implicit neural representations for the phase space coordinates, enabling a trainable embedding process. (b) Due to practical limitations, we have not yet verified our theory on very large-scale chaotic datasets. This aspect will

be left for our future research endeavors.

References

- [1] Bradley K Alpert. A class of bases in ℓ^2 for the sparse representation of integral operators. *SIAM journal on Mathematical Analysis*, 24(1):246–262, 1993.
- [2] Xueli An, Dongxiang Jiang, Chao Liu, and Minghao Zhao. Wind farm power prediction based on wavelet decomposition and chaotic time series. *Expert Systems with Applications*, 38(9):11280–11285, 2011.
- [3] Guy E Blelloch. Prefix sums and their applications. 1990.
- [4] Erik Bollt. On explaining the surprising success of reservoir computing forecaster of chaos? the universal machine learning dynamical system with contrast to var and dmd. *Chaos: An Interdisciplinary Journal of Nonlinear Science*, 31(1), 2021.
- [5] Minyou Chen, Yonghui Fang, and Xufei Zheng. Phase space reconstruction for improving the classification of single trial eeg. *Biomedical Signal Processing and Control*, 11:10–16, 2014.
- [6] Yen-Lin Chen, Yuan Chiang, Pei-Hsin Chiu, I-Chen Huang, Yu-Bai Xiao, Shu-Wei Chang, and Chang-Wei Huang. High-dimensional phase space reconstruction with a convolutional neural network for structural health monitoring. *Sensors*, 21(10):3514, 2021.
- [7] Mete Demircigil, Judith Heusel, Matthias Löwe, Sven Upgang, and Franck Vermet. On a model of associative memory with huge storage capacity. *Journal of Statistical Physics*, 168:288–299, 2017.
- [8] Robert Devaney. *An introduction to chaotic dynamical systems*. CRC press, 2018.
- [9] Ethan R Deyle and George Sugihara. Generalized theorems for nonlinear state space reconstruction. *Plos one*, 6(3):e18295, 2011.
- [10] Albert Gu and Tri Dao. Mamba: Linear-time sequence modeling with selective state spaces. *arXiv preprint arXiv:2312.00752*, 2023.
- [11] Albert Gu, Tri Dao, Stefano Ermon, Atri Rudra, and Christopher Ré. Hippo: Recurrent memory with optimal polynomial projections. *Advances in neural information processing systems*, 33:1474–1487, 2020.
- [12] Albert Gu, Karan Goel, and Christopher Ré. Efficiently modeling long sequences with structured state spaces. *arXiv preprint arXiv:2111.00396*, 2021.
- [13] Gaurav Gupta, Xiongye Xiao, and Paul Bogdan. Multiwavelet-based operator learning for differential equations. *Advances in neural information processing systems*, 34:24048–24062, 2021.
- [14] Varun Gupta, Monika Mittal, and Vikas Mittal. R-peak detection based chaos analysis of ecg signal. *Analog Integrated Circuits and Signal Processing*, 102:479–490, 2020.
- [15] Florian Hess, Zahra Monfared, Manuel Brenner, and Daniel Durstewitz. Generalized teacher forcing for learning chaotic dynamics. *arXiv preprint arXiv:2306.04406*, 2023.
- [16] John J Hopfield. Hopfield network. *Scholarpedia*, 2(5):1977, 2007.
- [17] Haowen Hou and F Richard Yu. Rwkv-ts: Beyond traditional recurrent neural network for time series tasks. *arXiv preprint arXiv:2401.09093*, 2024.
- [18] Jiayi Hu, Disen Lan, Ziyu Zhou, Qingsong Wen, and Yuxuan Liang. Time-ssm: Simplifying and unifying state space models for time series forecasting. *arXiv preprint arXiv:2405.16312*, 2024.
- [19] Jiayi Hu, Qingsong Wen, Sijie Ruan, Li Liu, and Yuxuan Liang. Twins: Revisiting non-stationarity in multivariate time series forecasting. *arXiv preprint arXiv:2406.03710*, 2024.

- [20] Ming Jin, Qingsong Wen, Yuxuan Liang, Chaoli Zhang, Siqiao Xue, Xue Wang, James Zhang, Yi Wang, Haifeng Chen, Xiaoli Li, et al. Large models for time series and spatio-temporal data: A survey and outlook. *arXiv preprint arXiv:2310.10196*, 2023.
- [21] H_S Kim, R Eykholt, and JD Salas. Nonlinear dynamics, delay times, and embedding windows. *Physica D: Nonlinear Phenomena*, 127(1-2):48–60, 1999.
- [22] Witold Kinsner. Characterizing chaos through lyapunov metrics. *IEEE Transactions on Systems, Man, and Cybernetics, Part C (Applications and Reviews)*, 36(2):141–151, 2006.
- [23] Yuxuan Liang, Haomin Wen, Yuqi Nie, Yushan Jiang, Ming Jin, Dongjin Song, Shirui Pan, and Qingsong Wen. Foundation models for time series analysis: A tutorial and survey. *arXiv preprint arXiv:2403.14735*, 2024.
- [24] Bryan Lim and Stefan Zohren. Time-series forecasting with deep learning: a survey. *Philosophical transactions. Series A, Mathematical, physical, and engineering sciences*, 379:20200209, 02 2021. doi: 10.1098/rsta.2020.0209.
- [25] Shengsheng Lin, Weiwei Lin, Wentai Wu, Feiyu Zhao, Ruichao Mo, and Haotong Zhang. Segrnn: Segment recurrent neural network for long-term time series forecasting. *arXiv preprint arXiv:2308.11200*, 2023.
- [26] Xu Liu, Junfeng Hu, Yuan Li, Shizhe Diao, Yuxuan Liang, Bryan Hooi, and Roger Zimmermann. Unitime: A language-empowered unified model for cross-domain time series forecasting. *arXiv preprint arXiv:2310.09751*, 2023.
- [27] Yong Liu, Tengge Hu, Haoran Zhang, Haixu Wu, Shiyu Wang, Lintao Ma, and Mingsheng Long. itransformer: Inverted transformers are effective for time series forecasting. *arXiv preprint arXiv:2310.06625*, 2023.
- [28] Yong Liu, Chenyu Li, Jianmin Wang, and Mingsheng Long. Koopa: Learning non-stationary time series dynamics with koopman predictors. *arXiv preprint arXiv:2305.18803*, 2023.
- [29] Yuqi Nie, Nam H Nguyen, Phanwadee Sinthong, and Jayant Kalagnanam. A time series is worth 64 words: Long-term forecasting with transformers. In *the Eleventh International Conference on Learning Representations (ICLR)*, 2023.
- [30] Lyle Noakes. The takens embedding theorem. *International Journal of Bifurcation and Chaos*, 1(04): 867–872, 1991.
- [31] Frank WJ Olver. *NIST handbook of mathematical functions hardback and CD-ROM*. Cambridge university press, 2010.
- [32] Sung Woo Park, Kyungjae Lee, and Junseok Kwon. Neural markov controlled sde: Stochastic optimization for continuous-time data. In *International Conference on Learning Representations*, 2021.
- [33] Milton Persson. The whitney embedding theorem, 2014.
- [34] Hubert Ramsauer, Bernhard Schödl, Johannes Lehner, Philipp Seidl, Michael Widrich, Thomas Adler, Lukas Gruber, Markus Holzleitner, Milena Pavlović, Geir Kjetil Sandve, et al. Hopfield networks is all you need. *arXiv preprint arXiv:2008.02217*, 2020.
- [35] Yulia Rubanova, Ricky TQ Chen, and David K Duvenaud. Latent ordinary differential equations for irregularly-sampled time series. *Advances in neural information processing systems*, 32, 2019.
- [36] Shahrokh Shahi, Flavio H Fenton, and Elizabeth M Cherry. Prediction of chaotic time series using recurrent neural networks and reservoir computing techniques: A comparative study. *Machine learning with applications*, 8:100300, 2022.
- [37] Jimmy TH Smith, Andrew Warrington, and Scott W Linderman. Simplified state space layers for sequence modeling. *arXiv preprint arXiv:2208.04933*, 2022.

- [38] I Vlachos and D Kugiumtzis. State space reconstruction for multivariate time series prediction. *arXiv preprint arXiv:0809.2220*, 2008.
- [39] Rui Wang, Yihe Dong, Sercan Ö Arik, and Rose Yu. Koopman neural forecaster for time series with temporal distribution shifts. *arXiv preprint arXiv:2210.03675*, 2022.
- [40] Zihan Wang, Fanheng Kong, Shi Feng, Ming Wang, Han Zhao, Daling Wang, and Yifei Zhang. Is mamba effective for time series forecasting? *arXiv preprint arXiv:2403.11144*, 2024.
- [41] Matthew O Williams, Ioannis G Kevrekidis, and Clarence W Rowley. A data-driven approximation of the koopman operator: Extending dynamic mode decomposition. *Journal of Nonlinear Science*, 25: 1307–1346, 2015.
- [42] Haixu Wu, Jiehui Xu, Jianmin Wang, and Mingsheng Long. Autoformer: Decomposition transformers with auto-correlation for long-term series forecasting. *Advances in Neural Information Processing Systems*, 34:22419–22430, 2021.
- [43] Haixu Wu, Tengge Hu, Yong Liu, Hang Zhou, Jianmin Wang, and Mingsheng Long. Timesnet: Temporal 2d-variation modeling for general time series analysis. *arXiv preprint arXiv:2210.02186*, 2022.
- [44] Ailing Zeng, Muxi Chen, Lei Zhang, and Qiang Xu. Are transformers effective for time series forecasting? In *Proceedings of AAAI*, volume 37, pages 11121–11128, 2023.
- [45] Tian Zhou, Ziqing Ma, Qingsong Wen, Liang Sun, Tao Yao, Wotao Yin, Rong Jin, et al. Film: Frequency improved legendre memory model for long-term time series forecasting. *Advances in Neural Information Processing Systems*, 35:12677–12690, 2022.
- [46] Tian Zhou, Ziqing Ma, Qingsong Wen, Xue Wang, Liang Sun, and Rong Jin. Fedformer: Frequency enhanced decomposed transformer for long-term series forecasting. In *International Conference on Machine Learning*, pages 27268–27286. PMLR, 2022.
- [47] Tian Zhou, Peisong Niu, xue wang, Liang Sun, and Rong Jin. One fits all: Power general time series analysis by pretrained lm. In *NeurIPS*, 2023.

A Technical Background

A.1 Taken Theorem

In the study of dynamic systems, a delay embedding theorem gives the conditions under which a chaotic dynamic system can be reconstructed from a sequence of observations of the state of that system. The reconstruction preserves the properties of the dynamic system that do not change under smooth coordinate changes (i.e., diffeomorphisms), but it does not preserve the geometric shape of structures in phase space.

Takens' theorem is the 1981 delay embedding theorem of Floris Takens. It provides the conditions under which a smooth attractor can be reconstructed from the observations made with a generic function. Later results replaced the smooth attractor with a set of arbitrary box counting dimension and the class of generic functions with other classes of functions.

It is the most commonly used method for attractor reconstruction. Delay embedding theorems are simpler to state for discrete-time dynamic systems. The state space of the dynamic system is a v -dimensional manifold \mathcal{M} . The dynamics is given by a smooth map

$$\mathcal{F} : M \rightarrow M$$

Assume that the dynamics \mathcal{F} has a strange attractor $\mathcal{A} \subset \mathcal{M}$ with box-counting dimension d_A . Using ideas from Whitney's embedding theorem [33], \mathcal{A} can be embedded in m -dimensional Euclidean space with

$$m > 2d_A.$$

That is, there is a diffeomorphism φ that maps \mathcal{A} into \mathbb{R}^N such that the derivative of φ has full rank. A delay embedding theorem uses an observation function to construct the embedding function. An observation function $h : \mathcal{M} \rightarrow \mathbb{R}$ must be twice-differentiable and associate a real number to any point of the attractor \mathcal{A} . It must also be typical, so its derivative is of full rank and has no special symmetries in its components. The delay embedding theorem states that the function

$$\varphi_T(x) = (h(x), h(\mathcal{F}(x)), \dots, h(\mathcal{F}^{k-1}(x)))$$

is an embedding of the strange attractor \mathcal{A} in \mathbb{R}^N .

Suppose the d -dimensional state vector x_t evolves according to an unknown but continuous and (crucially) deterministic dynamic. Suppose, too, that the one-dimensional observable y is a smooth function of x , and "coupled" to all the components of x . Now at any time we can look not just at the present measurement $y(t)$, but also at observations made at times removed from us by multiples of some lag $\tau : y_{t+\tau}, y_{t+2\tau}$, etc. If we use m lags, we have a m -dimensional vector. One might expect that, as the number of lags is increased, the motion in the lagged space will become more and more predictable, and perhaps in the limit $m \rightarrow \infty$ would become deterministic. In fact, the dynamics of the lagged vectors become deterministic at a finite dimension; not only that, but the deterministic dynamics are completely equivalent to those of the original state space (precisely, they are related by a smooth, invertible change of coordinates, or diffeomorphism). In fact, the theorem says that determinism appears once you reach dimension $2d + 1$, and the minimal embedding dimension is often less.

A.2 Hopfield Network

A.2.1 Classical Hopfield Network

A Hopfield network is a form of recurrent artificial neural network with binary neurons. It is characterized by:

- Binary neurons with states $+1$ or -1 .
- Symmetric weight matrix with zero diagonal (no self-connections).

- Energy function that is minimized at stable states.
- Asynchronous update of neuron states.

Dynamics

The state of each neuron is updated according to:

$$s_i(t+1) = \text{sign} \left(\sum_j w_{ij} s_j(t) \right) \quad (14)$$

Where $s_i(t+1)$ is the state of neuron i at time $t+1$, w_{ij} is the weight between neurons i and j , and $s_j(t)$ is the state of neuron j at time t .

The energy of the network is defined as:

$$E = -\frac{1}{2} \sum_{i,j} w_{ij} s_i s_j \quad (15)$$

Memory Storage and Retrieval

Memories are stored in the network by adjusting the weights to minimize the network energy, often using the Hebbian learning rule. The network can retrieve memory from a noisy or incomplete version by converging to a stored state. The memory capacity of a Hopfield network depends on several factors, with the most significant one being the number of neurons in the network. John Hopfield proposed a rule in his original paper to estimate the memory capacity, stating that the network can effectively store approximately $0.15N$ independent memories, where N represents the number of neurons in the network. This means that for a network containing 100 neurons, it can store approximately 15 patterns.

A.2.2 Modern Hopfield Network

In order to integrate Hopfield networks into deep learning architectures, The Modern Hopfield Network allows for continuous state updating. It proposes a new energy function based on the associative memory model [7] and proposes a new update rule that can be proven to converge to stationary points of the energy (local minima or saddle points). Specifically, the new Energy function is:

$$E = -\text{lse}(\beta, \mathbf{X}^T \boldsymbol{\xi}) + \frac{1}{2} \boldsymbol{\xi}^T \boldsymbol{\xi} + \beta^{-1} \log N + \frac{1}{2} M^2, \quad (16)$$

with $\text{lse}(\log - \text{sum} - \exp)$ interaction function:

$$\text{lse}(\beta, \mathbf{x}) = \beta^{-1} \log \left(\sum_{i=1}^N \exp(\beta x_i) \right) \quad (17)$$

Setting $0.5M^2$. Using $\mathbf{p} = \text{softmax}(\beta \mathbf{X}^T \boldsymbol{\xi})$, The novel update rule is:

$$\boldsymbol{\xi}^{\text{new}} = f(\boldsymbol{\xi}) = \mathbf{X} \mathbf{p} = \mathbf{X} \text{softmax}(\beta \mathbf{X}^T \boldsymbol{\xi}). \quad (18)$$

The new update rule can be viewed as the attention in Transformers. Firstly, N stored (key) patterns \mathbf{y}_i and S state (query) patterns \mathbf{r}_i that are mapped to the Hopfield space of dimension d_k . Then set $\mathbf{x}_i = \mathbf{W}_K^T \mathbf{y}_i$, $\boldsymbol{\xi}_i = \mathbf{W}_Q^T \mathbf{r}_i$, and multiply the result of the update rule with \mathbf{W}_V . The matrices $\mathbf{Y} = (\mathbf{y}_1, \dots, \mathbf{y}_N)^T$ and $\mathbf{R} = (\mathbf{r}_1, \dots, \mathbf{r}_S)^T$ combine the \mathbf{y}_i and \mathbf{r}_i as row vectors. By defining the matrices $\mathbf{X}^T = \mathbf{K} = \mathbf{Y} \mathbf{W}_K$, $\boldsymbol{\Xi}^T = \mathbf{Q} = \mathbf{R} \mathbf{W}_Q$, and $\mathbf{V} = \mathbf{Y} \mathbf{W}_K \mathbf{W}_V = \mathbf{X}^T \mathbf{W}_V$, where $\mathbf{W}_K \in \mathbb{R}^{d_y \times d_k}$, $\mathbf{W}_Q \in \mathbb{R}^{d_r \times d_k}$, $\mathbf{W}_V \in \mathbb{R}^{d_k \times d_v}$, $\beta = 1/\sqrt{d_k}$ and $\text{softmax} \in \mathbb{R}^N$ is changed to a row vector, the update rule multiplied by \mathbf{W}_V is:

$$\mathbf{Z} = \text{softmax} \left(1/\sqrt{d_k} \mathbf{Q} \mathbf{K}^T \right) \mathbf{V} = \text{softmax}(\beta \mathbf{R} \mathbf{W}_Q \mathbf{W}_K^T \mathbf{Y}^T) \mathbf{Y} \mathbf{W}_K \mathbf{W}_V.$$

In the Hopfield Evolution strategy of Attraos, The Query is settled as the dynamic structures and the Key/Value is settled as trainable vectors.

A.3 Orthogonal Polynomials

Note: In this section, we have selectively extracted key content from the appendix of Hippo [11] that is pertinent to our work, for the convenience of the reader. We take Legendre polynomials as an example.

Under the usual definition of the canonical Legendre polynomial P_n , they are orthogonal with respect to the measure $\omega^{\text{leg}} = \mathbf{1}_{[-1,1]}$:

$$\frac{2n+1}{2} \int_{-1}^1 P_n(x) P_m(x) dx = \delta_{nm}$$

Also, they satisfy

$$\begin{aligned} P_n(1) &= 1 \\ P_n(-1) &= (-1)^n. \end{aligned}$$

With respect to the measure $\frac{1}{\theta} \mathbb{I}[t - \theta, t]$, the normalized orthogonal polynomials are

$$(2n+1)^{1/2} P_n \left(2 \frac{x-t}{\theta} + 1 \right)$$

In general, the orthonormal basis for any uniform measure consists of $(2n+1)^{\frac{1}{2}}$ times the corresponding linearly shifted version of P_n .

Derivatives of Legendre polynomials We note the following recurrence relations on Legendre polynomials:

$$\begin{aligned} (2n+1)P_n &= P'_{n+1} - P'_{n-1} \\ P'_{n+1} &= (n+1)P_n + xP'_n \end{aligned}$$

The first equation yields

$$P'_{n+1} = (2n+1)P_n + (2n-3)P_{n-2} + \dots,$$

where the sum stops at P_0 or P_1 . These equations directly imply

$$P'_n = (2n-1)P_{n-1} + (2n-5)P_{n-3} + \dots$$

and

$$\begin{aligned} (x+1)P'_n(x) &= P'_{n+1} + P'_n - (n+1)P_n \\ &= nP_n + (2n-1)P_{n-1} + (2n-3)P_{n-2} + \dots \end{aligned}$$

To sum up, The Legendre polynomials are in closed-recursive form.

A.4 Piecewise Projection

Since the piecewise polynomial function space can be defined as the following form:

$$\mathcal{G}_{(r)}^k = \begin{cases} g \mid \deg(g) < k, & x \in (2^{-r}l, 2^{-r}(l+1)) \\ 0, & \text{otherwise} \end{cases}, \quad (19)$$

with polynomial order $k \in \mathbb{N}$, piecewise scale $r \in \mathbb{Z}^+ \cup \{0\}$, and piecewise internal index $l \in \{0, 1, \dots, 2^r - 1\}$, it is evident that $\dim(\mathcal{G}_{(r)}^k) = 2^r k$, implying that \mathcal{G}_{θ}^k possesses a superior function capacity compared to $\mathcal{G}_{2\theta}^k$. All functions in $\mathcal{G}_{2\theta}^k$ are encompassed within the domain of \mathcal{G}_{θ}^k . Moreover, since \mathcal{G}_{θ}^k and $\mathcal{G}_{2\theta}^k$ can be represented as space spanned by basis functions $\{\phi_i^{\theta}(x)\}$ and $\{\phi_i^{2\theta}(x)\}$, any function including the basis function within

the $\mathcal{G}_{2\theta}^k$ space can be precisely expressed as a linear combination of basis functions from the \mathcal{G}_θ^k space with a proper tilted measure $\mu_{2\theta}$:

$$\phi_i^{2\theta}(x) = \sum_{j=0}^{k-1} H_{ij}^{\theta_1} \phi_i^\theta(x)_{x \in [\theta_1]} + \sum_{j=0}^{k-1} H_{ij}^{\theta_2} \phi_i^\theta(x)_{x \in [\theta_2]}, \quad (20)$$

and back-projection can be achieved through the Moore-Penrose inverse H^\dagger . By taking the inner product with u on both sides in Eq. 20, we can project the state representation $x(t)$ between \mathcal{G}_θ^k space and the $\mathcal{G}_{2\theta}^k$ space.

B Proof

Proposition 5. [18] $\mathbf{A} = \text{diag}\{-1, -1, \dots\}$ is a rough approximation of shifted Hippo-LegT [11] matrix.

Proof. Hippo 3 provides a mathematical framework for deriving the \mathbf{AB} matrix for polynomial projection. The mainstream SSMs [10] typically initialize matrix $\mathbf{A} = \text{diag}\{-1, -2, -3, -4, \dots\}$, representing the negative real diagonal elements of the normalized Hippo-LegS matrix (21). Since the LegS matrix is a mathematical approximation of exponentially decaying Legendre polynomials, initializing $\mathbf{A} = \text{diag}\{-1, -2, -3, -4, \dots\}$ can be seen as a rough approximation of exponential decay. Similarly, for the normalized Hippo-LegT matrix (22), which approximates a uniform measure, we can consider $\mathbf{A} = \text{diag}\{-1, -1, \dots\}$ as a rough approximation of a finite window of Legendre polynomials, which better for non-stationary time series as well [19]. The use of negative values for the elements is to ensure gradient stability during training.

$$\begin{aligned} \mathbf{A}_{nk}^{(N)} &= - \begin{cases} (n + \frac{1}{2})^{1/2} (k + \frac{1}{2})^{1/2} & n > k \\ \frac{1}{2} & n = k \\ (n + \frac{1}{2})^{1/2} (k + \frac{1}{2})^{1/2} & n < k \end{cases} \quad (21) \\ \mathbf{A} &= \mathbf{A}^{(N)} - \text{rank}(1), \quad \mathbf{A}^{(D)} := \text{eig}(\mathbf{A}^{(N)}) \\ &\text{(Normal / DPLR form of HiPPO-LegS)} \end{aligned} \quad \begin{aligned} \mathbf{A}_{nk}^{(N)} &= - \begin{cases} (2n+1)^{\frac{1}{2}} (2k+1)^{\frac{1}{2}} & n < k, k \text{ odd} \\ 0 & \text{else} \\ (2n+1)^{\frac{1}{2}} (2k+1)^{\frac{1}{2}} & n > k, n \text{ odd} \end{cases} \\ \mathbf{A} &= \mathbf{A}^{(N)} - \text{rank}(2), \quad \mathbf{A}^{(D)} := \text{eig}(\mathbf{A}^{(N)}) \\ &\text{(Normal / DPLR form of HiPPO-LegT)} \end{aligned} \quad (22)$$

□

Theorem 6. (Approximation Error Bound) Suppose that the function $f : [0, 1] \in \mathbb{R}$ is k times continuously differentiable, the piecewise polynomial g approximates f with mean error bounded as follows:

$$\|f - g\| \leq 2^{-rk} \frac{2}{4^N k!} \sup_{x \in [0, 1]} |f^{(k)}(x)|.$$

Proof. Similar to [1], we divide the interval $[0, 1]$ into subintervals on which g is a polynomial; the restriction of g to one such subinterval $I_{r,l}$ is the polynomial of degree less than k that approximates f with minimum mean error. Also, the optimal g can be regarded as the orthonormal projection $Q_r^N f$ onto $\mathcal{G}_{(r)}^N$. We then use the maximum error estimate for the polynomial, which interpolates f at Chebyshev nodes of order k on $I_{r,l}$.

We define $I_{r,l} = [2^{-r}l, 2^{-r}(l+1)]$ for $l = 0, 1, \dots, 2^r - 1$, and obtain

$$\begin{aligned}
\|Q_r^N f - f\|^2 &= \int_0^1 [(Q_r^N f)(x) - f(x)]^2 dx \\
&= \sum_l \int_{I_{r,l}} [(Q_r^N f)(x) - f(x)]^2 dx \\
&\leq \sum_l \int_{I_{r,l}} [(C_{r,l}^N f)(x) - f(x)]^2 dx \\
&\leq \sum_l \int_{I_{r,l}} \left(\frac{2^{1-rk}}{4^N k!} \sup_{x \in I_{r,l}} |f^{(k)}(x)| \right)^2 dx \\
&\leq \left(\frac{2^{1-rk}}{4^N k!} \sup_{x \in [0,1]} |f^{(k)}(x)| \right)^2
\end{aligned}$$

and by taking square roots we have bound (7). Here $C_{r,l}^N f$ denotes the polynomial of degree k which agrees with f at the Chebyshev nodes of order k on $I_{r,l}$, and we have used the well-known maximum error bound for Chebyshev interpolation.

The error of the approximation $Q_r^N f$ of f therefore decays like 2^{-rk} and, since S_r^N has a basis of $2^r k$ elements, we have convergence of order k . For the generalization to m dimensions in the dynamic structure modeling, a similar argument shows that the rate of convergence is of order k/m . \square

Theorem 7. (Evolution Error Bound) *By Jacobian value, the mean attractor evolution error $\|\mathcal{K} \circ \tilde{\mathcal{A}} - \tilde{\mathcal{A}}\|$ of evolution operator $\mathcal{K} = \{\mathcal{K}^{(i)}\}$ is bounded by*

$$\|\mathcal{K} \circ \tilde{\mathcal{A}} - \tilde{\mathcal{A}}\| (N-1) \mathcal{E}(-\beta \nabla_i + 1)$$

with the number of random patterns $N \geq \sqrt{pc} \frac{d-1}{4}$ stored in the system by interaction paradigm \mathcal{E} in an ideal spherical retrieval paradigm.

Proof. Due to the numerous assumptions and extensive lemmas involved in the proof of this theorem, we will provide a brief exposition of its main ideas. For a detailed proof, please refer to [34].

Firstly, the theorem defines the matching between patterns as:

Definition 1. (Pattern match). *Assuming that around every pattern \mathbf{x}_i a sphere S_i is given. We say \mathbf{x}_i is matched with $\boldsymbol{\xi}$ if there is a single fixed point $\mathbf{x}_i^* \in S_i$ to which all points $\boldsymbol{\xi} \in S_i$ converge.*

As shown in **Theorem 3** in [34], according to the upper branch of the Lambert W function [31], we can obtain the number of random patterns stored in a system is $N \geq \sqrt{pc} \frac{d-1}{4}$.

In our paper, we define the pattern1 as the Attractor $\tilde{\mathcal{A}}$ in phase space, pattern2 as the future state evaluated by operator \mathcal{K} , noted as $\mathcal{K} \circ \tilde{\mathcal{A}}$. From **Lemma A4** in [34], when the radius of the pattern matching sphere is M , we can describe the evolution process by jacobian value and get the matching error as:

$$\|\mathcal{K} \circ \tilde{\mathcal{A}} - \tilde{\mathcal{A}}\| 2\epsilon M$$

where in the **Equation (179)** of [34]:

$$\epsilon = (N-1) \exp \left(-\beta \left(\nabla_i - 2 \max \left\{ \|\mathcal{K} \circ \tilde{\mathcal{A}} - \tilde{\mathcal{A}}\|, \|\tilde{\mathcal{A}}_i^* - \tilde{\mathcal{A}}_i\| \right\} M \right) \right).$$

The **Equation (404)** of [34] says $\|\tilde{\mathcal{A}}_i^* - \tilde{\mathcal{A}}_i\| \frac{1}{2\beta M}$ and $\|\mathcal{K} \circ \tilde{\mathcal{A}} - \tilde{\mathcal{A}}\| \frac{1}{2\beta M}$, so we can get:

$$\epsilon \exp(N-1) M \exp(-\beta \nabla_i).$$

In our paper, we replace the exponential interaction function with an unknown function $\mathcal{E}(\cdot)$ to finally get the version in Theorem 3. □

Theorem 8. (Completeness in L^2 space) *The orthonormal system $B_k = \{\phi_j : j = 1, \dots, k\} \cup \{\psi_j^{rl} : j = 1, \dots, k; r = 0, 1, 2, \dots; l = 0, \dots, 2^r - 1\}$ spans $L^2[0, 1]$.*

Proof. We define the space \mathcal{G}^N to be the union of the $\mathcal{G}_{(r)}^N$, given by the formula:

$$\mathcal{G}^N = \bigcup_{r=0}^{\infty} \mathcal{G}_r^N \quad (23)$$

and observe that $\overline{\mathcal{G}^N} = L^2[0, 1]$. In particular, \mathcal{G}^N contains the Haar basis for $L^2[0, 1]$, consisting of functions piecewise constant on each of the subintervals $(2^{-r}l, 2^{-r}(l+1))$. Here the closure $\overline{\mathcal{G}^N}$ is defined with respect to the L^2 -norm,

$$\|f\| = \langle f, f \rangle^{1/2}$$

where the inner product $\langle f, g \rangle$ is defined by the formula

$$\langle f, g \rangle = \int_0^1 f(x)g(x)dx.$$

Also, we have:

$$\mathcal{G}_r^N = \mathcal{G}_0^N \oplus \mathcal{S}_0^N \oplus \mathcal{S}_1^N \oplus \dots \oplus \mathcal{S}_{r-1}^N \quad (24)$$

and

$$\mathcal{S}_r^N = \text{linear span } \{\psi_{j,r}^l : \psi_{j,r}^l(x) = 2^{r/2}\psi_j(2^r x - l), j = 1, \dots, k; n = 0, \dots, 2^r - 1\}. \quad (25)$$

We let $\{\phi_1, \dots, \phi_k\}$ denote an orthonormal basis for \mathcal{G}_0^N ; in view of Equation 23, 24, and 25, the orthonormal system

$$B_k = \bigcup \left\{ \begin{array}{ll} \phi_j : & j = 1, \dots, k \\ \psi_{j,r}^l : & j = 1, \dots, k; r = 0, 1, 2, \dots; l = 0, \dots, 2^r - 1 \end{array} \right\}$$

spans $L^2[0, 1]$.

Now we construct a basis for $L^2(\mathbf{R})$ by defining, for $r \in \mathbf{Z}$, the space $\tilde{\mathcal{G}}_r^N$ by the formula $\tilde{\mathcal{G}}_r^N = \{f : \text{the restriction of } f \text{ to the interval } (2^{-r}n, 2^{-r}(n+1)) \text{ is a polynomial of degree less than } k, \text{ for } n \in \mathbf{Z}\}$ and observing that the space $\tilde{\mathcal{G}}_{r+1}^N \setminus \tilde{\mathcal{G}}_r^N$ is spanned by the orthonormal set

$$\left\{ \psi_{j,r}^l : \psi_{j,r}^l(x) = 2^{r/2}\psi_j(2^r x - l), j = 1, \dots, k; l \in \mathbf{Z} \right\}.$$

Thus $L^2(\mathbf{R})$, which is contained in $\overline{\bigcup_r \tilde{\mathcal{G}}_r^N}$, has an orthonormal basis

$$\{\psi_{j,m}^n : j = 1, \dots, k; r, l \in \mathbf{Z}\}$$

□

C Model Details

C.1 Phase Space Reconstruction

Phase space reconstruction is a crucial technique in the analysis of dynamic systems, particularly in the study of time series data. This method transforms a one-dimensional time series into a multidimensional phase space, revealing the underlying dynamics of the system. The cross-correlation mutual information (CC mutual information) method is a statistical tool used to analyze the dependencies between two different time series. We provide a detailed mathematical description of these methods.

Phase space reconstruction involves transforming a single-variable time series into a multidimensional space to unveil the dynamics of the system that generated the data. The technique is based on Takens' Embedding Theorem.

Takens' Embedding Theorem

Takens' Embedding Theorem allows the reconstruction of a dynamic system's phase space from a sequence of observations. The theorem states that under generic conditions, a map:

$$F : \mathbb{R}^n \rightarrow \mathbb{R}^m \quad (26)$$

can be constructed, where n is the dimension of the original phase space, and m is the embedding dimension, typically $m \leq 2n + 1$ is sufficient to recover dynamics.

Time Delay Embedding

The most common approach for phase space reconstruction is the time delay embedding method. Given a time series $\{x(t)\}$, the reconstructed phase space is:

$$X(t) = [x(t), x(t + \tau), x(t + 2\tau), \dots, x(t + (m - 1)\tau)] \quad (27)$$

where τ is the time delay, and m is the embedding dimension. In the context of coordinate delay reconstruction in a complete scenario, it involves a parameter called time window, which selectively uses discrete one-dimensional data for phase space reconstruction. In order to maximize the preservation of time series information, the time window parameter is typically set to 1. As a result, this process is reversible, meaning that the original data can be reconstructed without loss of information.

The CC mutual information method is used to analyze the dependencies between two time series. It is a measure of the amount of information obtained about one time series through the other.

Mutual Information

Mutual information $I(X; Y)$ between two random variables X and Y is defined as:

$$I(X; Y) = \sum_{x \in X, y \in Y} p(x, y) \log \frac{p(x, y)}{p(x)p(y)} \quad (28)$$

where $p(x, y)$ is the joint probability distribution function of X and Y , and $p(x)$ and $p(y)$ are the marginal probability distribution functions.

Cross-Correlation Mutual Information

For time series analysis, the mutual information is extended to account for the time-lagged relationships:

$$I(X; Y, \tau) = \sum_{x \in X, y \in Y} p(x, y(\tau)) \log \frac{p(x, y(\tau))}{p(x)p(y(\tau))} \quad (29)$$

where τ is the time lag, and $y(\tau)$ represents the time series Y shifted by τ .

Determining Time Delay (τ)

Time delay (τ) is an interval used in reconstructing the phase space of a time series. The right choice of τ is essential for revealing the dynamic properties of the system.

Calculating Mutual Information

For a given time series $\{x_t\}$, calculate the mutual information between the time series and its time-shifted version for different delays τ :

$$I(\tau) = \sum p(x_t, x_{t+\tau}) \log \left(\frac{p(x_t, x_{t+\tau})}{p(x_t)p(x_{t+\tau})} \right) \quad (30)$$

where $p(x_t, x_{t+\tau})$ is the joint probability distribution, and $p(x_t)$ and $p(x_{t+\tau})$ are the marginal probability distributions.

Selecting Time Delay

Plot the mutual information $I(\tau)$ against τ . Choose the τ at the first local minimum of this plot. This represents the delay where the series' points provide maximal mutual information.

Determining Embedding Dimension (m)

Embedding dimension (m) is the dimension of the reconstructed phase space. The correct m ensures that trajectories in the phase space do not intersect each other.

Calculating False Nearest Neighbors

For each dimension m , calculate the false nearest neighbors (FNN) $F(m)$, which reflects the complexity of the trajectories reconstructed in m -dimensional space:

$$F(m) = \left(\frac{1}{N - m + 1} \sum_{i=1}^{N-m+1} \log C_i(m, r) \right) \quad (31)$$

where $C_i(m, r)$ is the count of points within a distance r from point i in m -dimensional space, and N is the length of the time series.

Identifying the Saturation Point

As m increases, $F(m)$ typically increases and reaches a saturation point. Choose the smallest m for which $F(m)$ does not significantly increase, indicating that increasing the dimension does not reveal more information about the dynamics.

D Experiments Details

D.1 Datasets

Our experiments are carried out on Five real-world datasets and two chaos datasets as described below:

- **ETT**¹ dataset are procured from two electricity substations over two years. They provide a summary of load and oil temperature data across seven variables. For ETTm1 and ETTm2, the "m" signifies that data was recorded every 15 minutes, yielding 69,680 time steps. ETTh1 and ETTh2 represent the hourly equivalents of ETTm1 and ETTm2, each containing 17,420 time steps.
- **Exchange**² dataset details the daily foreign exchange rates of eight countries, including Australia, British, Canada, Switzerland, China, Japan, New Zealand, and Singapore from 1990 to 2016.

¹<https://github.com/zhouhaoyi/ETDataset>

²<https://github.com/laiguokun/multivariate-time-series-data>

- **Weather**³ dataset is a meteorological collection featuring 21 variates, gathered in the United States over a four-year span.
- **Lorenz96** dataset is an artificial dataset. We simulate the data of 30,000 time steps with an initial dimension of 40d according to the Lorenz96 equation and map to 3D by a randomly initialized Linear network to simulate the realistic chaotic time series generated from an unknown underlying chaotic system. More details are in Appendix E.3.
- **Cryptots** comprises historical transaction data for various cryptocurrencies, including Bitcoin and Ethereum. We select samples with *Asset_ID* set to 0, and remove the column *Count*. We download the data from https://www.kaggle.com/competitions/g-research-crypto-forecasting/data?select=supplemental_train.csv.
- **Air Convection**⁴ dataset is obtained by scraping the data from NOAA, and it includes the data for the entire year of 2023. The dataset consists of 20 variables, including air humidity, pressure, convection characteristics, and others. The data was sampled at intervals of 15 minutes and averaged over the course of the entire year.
- **Lorenz96-3d**: See Appendix E.3.

D.2 Baselines

Our baseline models include: **Mamba4TS**: Mamba4TS is a novel SSM architecture tailored for TSF tasks, featuring a parallel scan (<https://github.com/alxndrTL/mamba.py/tree/main>). Additionally, this model adopts a patching operation with both patch length and stride set to 16. We use the recommended configuration as our experimental settings with a batch size of 32, and the learning rate is 0.0001.

S-Mamba [40]: S-Mamba utilizes a linear tokenization of variates and a bidirectional Mamba layer to efficiently capture inter-variate correlations and temporal dependencies. This approach underscores its potential as a scalable alternative to Transformer technologies in TSF. We download the source code from: <https://github.com/wzhwzhwzh0921/S-D-Mamba> and adopt the recommended setting as its experimental configuration.

RWKV-TS [17]: RWKV-TS is an innovative RNN-based architecture for TSF that offers linear time and memory efficiency. We download the source code from: <https://github.com/howard-hou/RWKV-TS>. We follow the recommended settings as experimental configuration.

Koopa [28]: Koopa is a novel forecasting model that tackles non-stationary time series using Koopman theory to differentiate time-variant dynamics. It features a Fourier Filter and Koopman Predictors within a stackable block architecture, optimizing hierarchical dynamics learning. We download the source code from: <https://github.com/thuml/Koopa>. We set the lookback window to fixed values of {96, 192, 336, 720} instead of twice the output length as in the original experimental settings.

iTransformer [27]: iTransformer modifies traditional Transformer models for time series forecasting by inverting dimensions and applying attention and feed-forward networks across variate tokens. We download the source code from: <https://github.com/thuml/iTransformer>. We follow the recommended settings as experimental configuration.

PatchTST [29]: PatchTST introduces a novel design for Transformer-based models tailored to time series forecasting. It incorporates two essential components: patching and channel-independent structure. We obtain the source code from: <https://github.com/PatchTST>. This code serves as our baseline for long-term forecasting, and we follow the recommended settings for our experiments.

LTSF-Linear [44]: In LTSF-Linear family, DLinear decomposes raw data into trend and seasonal components and NLinear is just a single linear models to capture temporal relationships between input and output

³<https://www.bgc-jena.mpg.de/wetter>

⁴<https://www.psl.noaa.gov/>

sequences. We obtain the source code from: <https://github.com/cure-lab/LTSF-Linear>, using it as our long-term forecasting baseline and adhering to recommended settings for experimental configuration.

GPT4TS [47]: This study explores the application of pre-trained language models to time series analysis tasks, demonstrating that the Frozen Pretrained Transformer (FPT), without modifications to its core architecture, achieves state-of-the-art results across various tasks. We download the source code from: <https://github.com/DAMO-DI-ML/NeurIPS2023-One-Fits-All>. We follow the recommended settings as experimental configuration.

D.3 Experiments Setting

All experiments are conducted on the NVIDIA RTX3090-24G and A6000-48G GPUs. The Adam optimizer is chosen. A grid search is performed to determine the optimal hyperparameters, including the learning rate from $\{0.0001, 0.0005, 0.001\}$, polynomial order from $\{32, 64, 256\}$, patch length from $\{8, 16\}$, projection level based on $\log L$ and no more than 3, and primary modes from $\{32, 64\}$. The input length is 96. Due to the sensitivity of the CC method to numerical calculations, we take the average result from three iterations of the calculation.

E Supplemental Experiments

E.1 Dynamic Structures of Real-world Data

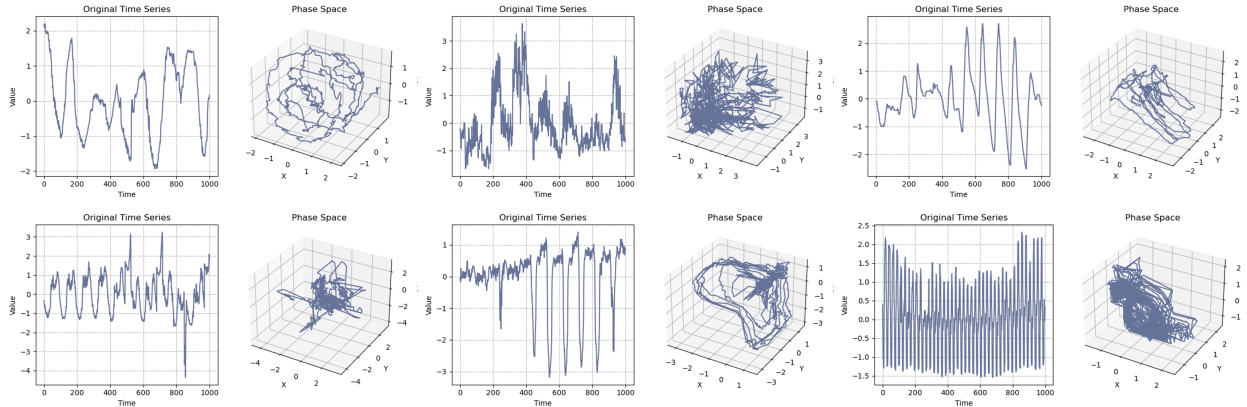


Figure 5: Dynamic structures of real-world data

As shown in Figure 5, we present the phase space structures of various real-time series. Please note that due to our visualization limitations in three dimensions, the shapes of many attractors for these time series are manifested in higher dimensions. We can only display slices of the attractors in the first three dimensions.

E.2 The Chaotic Nature of Datasets

Lyapunov Exponent

Lyapunov exponents are a set of quantities that characterize the rate of separation of infinitesimally close trajectories in a dynamic system. They play a crucial role in understanding the stability and chaotic behavior of the system [22]. The formal definition of the Lyapunov exponent for a trajectory of a dynamic system is given by:

$$\lambda = \lim_{t \rightarrow \infty} \frac{1}{t} \ln \left(\frac{\|\delta X_i(t)\|}{\|\delta X_i(0)\|} \right), \quad (32)$$

where $\delta\mathbf{X}(t)$ is the deviation vector at time t , and λ is the Lyapunov exponent. The set of Lyapunov exponents for a system provides a spectrum, indicating the behavior of trajectories in each dimension of the system’s phase space.

When the direction of the initial separation vector is different, the separation rate is also different. Thus, the spectrum of Lyapunov exponents exists, which have the same number of dimensions as the phase space. The largest of these is often referred to as the Maximal Lyapunov exponent (MLE). We reconstruct dimension m according to different phase spaces to get the maximum Lyapunov index. A positive MLE is often considered an indicator of chaotic behavior in the system, while a negative value indicates convergence, implying stability in the system’s behavior.

As shown in Table 6, we calculate the maximum Lyapunov exponent for all mainstream LTSF datasets. Surprisingly, we find that their MLEs are all positive, indicating the presence of chaos to varying degrees in these datasets. This directly supports the motivation proposed by Attraos. Among them, the weather dataset exhibits the strongest chaotic behavior. Note that the existence of at least one positive Lyapunov exponent is sufficient to determine the presence of chaos. For example, the classical Lorenz63 system has three Lyapunov exponents with values negative, zero, and positive respectively.

Remark E.1. *For multivariate time series, we take the average.*

Table 6: Maximal Lyapunov Exponents for Various Datasets in Multivariate Long-Term Forecasting

Dataset	ETTh1	ETTh2	ETTm1	ETTm2	Exchange	Weather	Electricity	Traffic
MLE	0.064437	0.059833	0.071673	0.082791	0.039670	0.242649	0.014613	0.189311

E.3 Simulation for Lorenz96 (Case Study)

Lorenz63 System

The Lorenz ’63 model, introduced by Edward Lorenz in 1963, is a simplified mathematical model for atmospheric convection. The model is a system of three ordinary differential equations now known as the Lorenz equations:

$$\frac{dx}{dt} = \sigma(y - x), \quad (33)$$

$$\frac{dy}{dt} = x(\rho - z) - y, \quad (34)$$

$$\frac{dz}{dt} = xy - \beta z. \quad (35)$$

Here, x , y , and z make up the state of the system. The parameters σ , ρ , and β represent the Prandtl number, Rayleigh number, and certain physical dimensions of the layer, respectively. Lorenz derived these equations to model the way air moves around in the atmosphere. This model is famous for exhibiting chaotic behavior for certain parameter values and initial conditions.

Lorenz96 System

The Lorenz96 system is a mathematical model that was introduced by Edward N. Lorenz in 1996 as an extension of the original Lorenz model. It is commonly used to study chaotic dynamics in systems with multiple interacting variables.

The Lorenz96 system consists of a set of ordinary differential equations that describe the time evolution of a set of variables. In its simplest form, the system is defined as follows:

$$\frac{dx_i}{dt} = (x_{i+1} - x_{i-2})x_{i-1} - x_i + F$$

Here, x_i represents the state variable at position i , and F is a forcing term that controls the overall behavior of the system. The nonlinear term $(x_{i+1} - x_{i-2})x_{i-1}$ captures the interactions between neighboring variables,

leading to the emergence of chaotic behavior. The Lorenz96 system exhibits a range of fascinating phenomena, including intermittent chaos, phase transitions, and the presence of multiple stable and unstable regimes. Its dynamics have been extensively studied to gain insights into the behavior of complex systems and to explore the limits of predictability.

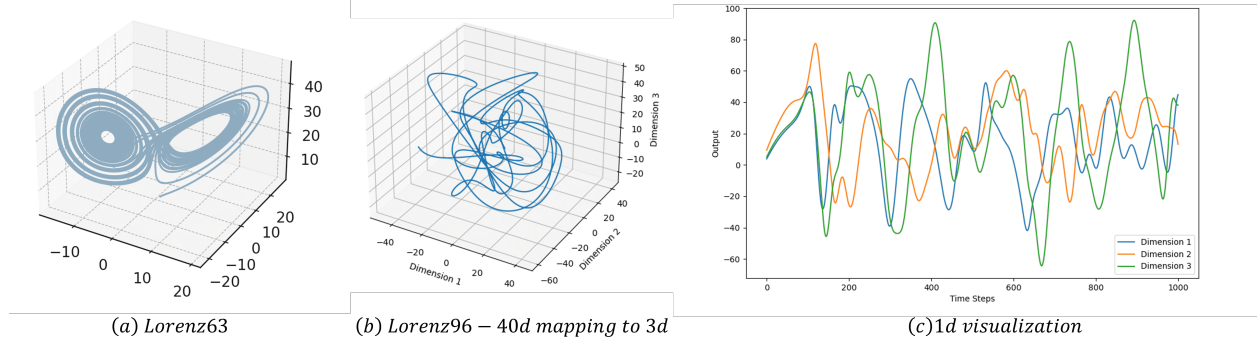


Figure 6: Simulation for Lorenz96

To simulate time series generated from an unknown chaotic system, we first construct a 40-dimensional Lorenz96 system to represent the underlying chaotic system. We then use a randomly initialized linear neural network to simulate the observation function h . Through h , we map the Lorenz96-40d system, which resides in the manifold space, to a 3-dimensional Euclidean space to obtain a multivariate time series dataset with three variables. As shown in the middle of Figure 6, in the observation domain, the dynamic system structure of Lorenz96-40d is difficult to discern specific shapes, so we need to reconstruct it to 40 dimensions using the Phase Space Reconstruction (PSR) technique to study its dynamic characteristics in a topologically equivalent structure. It is worth noting that on the right side of Figure 6, we visualize the last variable of the system and find striking similarities with real-world time series, even exhibiting some periodic behaviors. This further supports our hypothesis that real-world time series are generated by underlying chaotic systems.

E.4 Chaotic Modulation

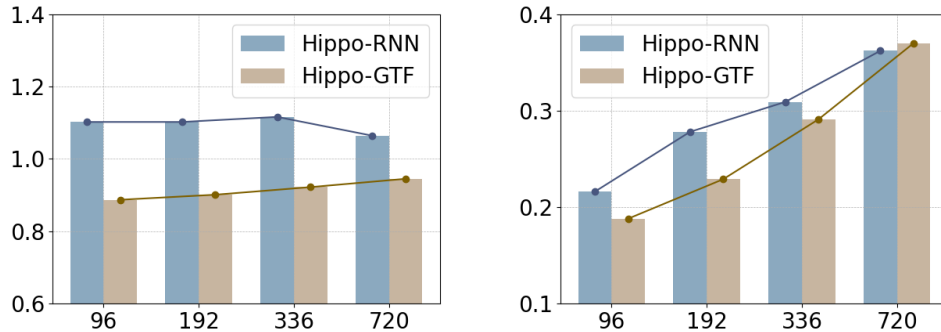


Figure 7: Performance comparison about teaching forcing, measured by MSE. Left: Lorenz96 dataset. Right: Weather dataset.

In LTSF tasks, it is commonly observed that predictive performance deteriorates as the length of the forecasting window increases. This phenomenon bears a striking resemblance to the inherent challenge in long-term predictions of chaotic dynamic systems, which are highly sensitive to initial conditions. Recent studies [15] in the field of chaotic dynamic systems have highlighted that, to address the issue of gradient divergence caused by positive maximal Lyapunov exponents indicative of chaos, the implementation of teaching forcing as a method to incrementally constrain the trajectory of the dynamic system presents a straightforward yet effective framework. To enhance Hippo-RNN, we have implemented the following

modifications: $\tilde{z}_t := (1 - \alpha)z_t + \alpha\bar{z}_t$, $z_t = \mathbf{F}_\theta(\tilde{z}_{t-1})$, with $0 \leq \alpha \leq 1$, where we intervene the evolution state z by utilizing the ground truth hidden state \bar{z} . As shown in Figure 7, this modification leads to notable improvements in both mainstream LTSF datasets and real-world chaotic datasets. However, the autoregressive nature of the teaching forcing methods introduces additional computational overhead and may potentially reduce its generalization capabilities, which presents a challenge for integrating it into sequence-mapping models.

E.5 Chaotic Reconstruction

As illustrated in Figure 8, we visualize the phase space forecasting results of Attraos on the Lorenz96 system. It can be observed that: Although some minor details may be missing due to the sparsity introduced by the frequency domain evolution, Attraos successfully reconstructs the chaotic dynamic structure of Lorenz96. Moreover, modeling time series based on the dynamics structure of the phase space can be viewed as a form of data augmentation, e.g., two-dimensional time figuring [43] or seasonal decomposition [46].

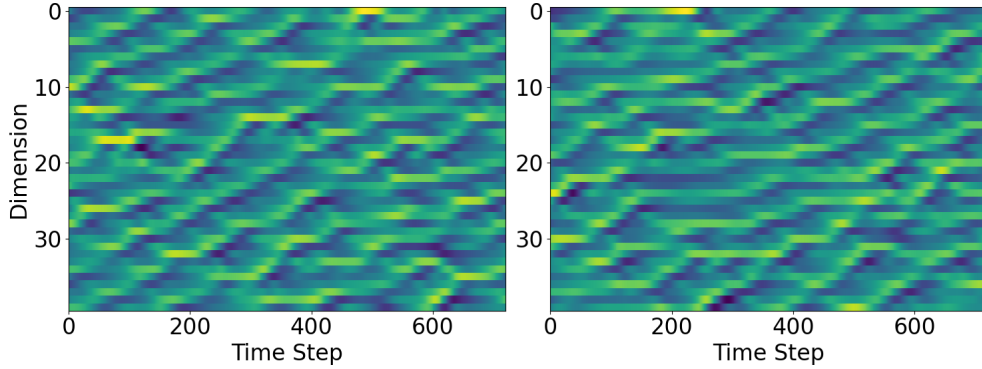


Figure 8: Chaotic reconstruction process for Lorenz96-40d. Left: Ground truth. Right: Prediction.

E.6 Chaos Representation (Hyper-parameter Analysis)

We validated the impact of polynomial dimensions on the model performance and observed that the chunking operation significantly reduces the reliance on polynomial space dimensions, thereby greatly reducing the number of model parameters.

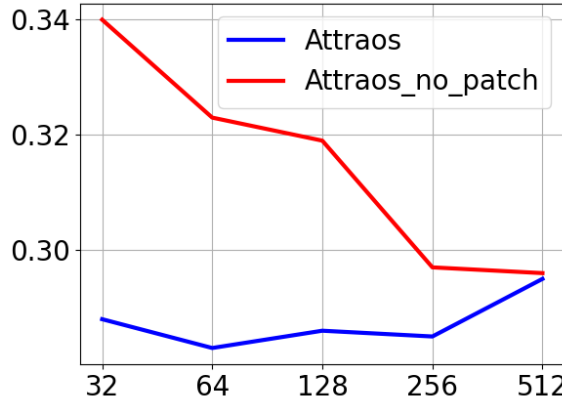


Figure 9: Hyper-parameter analysis, the X-axis is polynomial order. Metric is MSE in ETTm2 dataset.

E.7 Full Results

As shown in Table 7, we showcase the full experiment results for all mainstream LTSF datasets.

Table 7: Multivariate long-term series forecasting results in mainstream datasets with input length is 96 and prediction horizons are {96, 192, 336, 720}. The best model is in boldface, and the second best is underlined. The bottom part introduces the variable Kernel for multivariate variables.

Model		Attrasos (Ours)		Mamba4TS (Temporal Emb.)		S-Mamba (Channel Emb.[40])		RWKV-TS [17]		GPT4TS [47]		Koopas [28]		InvTrm [27]		PatchTST [29]		DLinear [44]	
Metric		MSE	MAE	MSE	MAE	MSE	MAE	MSE	MAE	MSE	MAE	MSE	MAE	MSE	MAE	MSE	MAE	MSE	MAE
ETTth1	96	0.370	0.388	0.386	0.400	0.388	0.407	0.383	0.401	0.398	0.424	0.385	0.408	0.393	0.409	0.375	0.396	0.396	0.410
	192	0.416	0.418	0.426	0.430	0.443	0.439	0.441	0.431	0.441	0.436	0.441	0.431	0.448	0.442	0.429	0.426	0.449	0.444
	336	0.458	0.432	0.484	0.451	0.492	0.467	0.493	0.465	0.492	0.466	0.474	0.454	0.491	0.465	0.461	0.448	0.487	0.465
	720	0.447	0.442	0.481	0.472	0.511	0.499	0.501	0.487	0.487	0.483	0.501	0.480	0.518	0.501	0.469	0.471	0.515	0.512
	AVG	0.423	0.420	0.444	0.438	0.459	0.453	0.454	0.446	0.457	0.450	0.450	0.443	0.463	0.454	0.434	0.435	0.462	0.458
ETTth2	96	0.292	0.348	0.297	0.347	0.296	0.347	0.290	0.342	0.312	0.360	0.317	0.359	0.302	0.351	0.295	0.344	0.353	0.405
	192	0.374	0.386	0.392	0.409	0.377	0.398	0.372	0.393	0.387	0.405	0.375	0.399	0.379	0.399	0.375	0.399	0.482	0.479
	336	0.420	0.432	0.424	0.436	0.425	0.435	0.417	0.431	0.424	0.437	0.436	0.446	0.423	0.432	0.420	0.429	0.588	0.539
	720	0.418	0.431	0.431	0.448	0.427	0.446	0.421	0.442	0.433	0.453	0.460	0.463	0.429	0.447	0.431	0.451	0.833	0.658
	AVG	0.376	0.399	0.386	0.410	0.381	0.407	0.375	0.402	0.389	0.414	0.397	0.417	0.383	0.407	0.380	0.406	0.564	0.520
ETTm1	96	0.321	0.362	0.331	0.368	0.332	0.368	0.328	0.366	0.335	0.369	0.322	0.360	0.343	0.377	0.326	0.365	0.345	0.372
	192	0.365	0.373	0.376	0.391	0.378	0.393	0.372	0.389	0.374	0.385	0.378	0.393	0.379	0.394	0.261	0.383	0.382	0.391
	336	0.390	0.395	0.406	0.413	0.409	0.414	0.401	0.409	0.407	0.406	0.405	0.413	0.418	0.418	0.396	0.405	0.413	0.413
	720	0.451	0.432	0.469	0.452	0.476	0.453	0.462	0.446	0.469	0.442	0.473	0.447	0.488	0.458	0.458	0.439	0.472	0.450
	AVG	0.382	0.391	0.396	0.406	0.399	0.407	0.391	0.403	0.396	0.401	0.395	0.403	0.407	0.412	0.403	0.398	0.403	0.406
ETTm2	96	0.172	0.254	0.186	0.268	0.182	0.267	0.181	0.264	0.190	0.275	0.180	0.261	0.184	0.269	0.177	0.260	0.192	0.291
	192	0.242	0.301	0.261	0.320	0.248	0.309	0.245	0.307	0.253	0.313	0.244	0.304	0.253	0.313	0.246	0.308	0.284	0.360
	336	0.303	0.340	0.331	0.366	0.312	0.350	0.306	0.344	0.321	0.360	0.300	0.340	0.313	0.351	0.302	0.343	0.371	0.420
	720	0.401	0.399	0.418	0.416	0.412	0.406	0.406	0.406	0.411	0.406	0.398	0.400	0.413	0.406	0.407	0.405	0.532	0.511
	AVG	0.280	0.324	0.299	0.343	0.289	0.333	0.285	0.330	0.294	0.339	0.281	0.326	0.291	0.335	0.283	0.329	0.345	0.396
Exchange	96	0.082	0.200	0.086	0.205	0.087	0.209	0.129	0.256	0.091	0.212	0.093	0.215	0.097	0.222	0.093	0.212	0.094	0.227
	192	0.171	0.294	0.173	0.297	0.180	0.303	0.231	0.346	0.183	0.304	0.189	0.313	0.184	0.309	0.201	0.319	0.185	0.325
	336	0.331	0.415	0.340	0.423	0.330	0.417	0.380	0.448	0.328	0.417	0.371	0.443	0.327	0.416	0.338	0.422	0.330	0.437
	720	0.810	0.669	0.855	0.696	0.860	0.700	0.883	0.704	0.880	0.704	0.908	0.726	0.885	0.715	0.900	0.711	0.774	0.673
	AVG	0.349	0.395	0.364	0.405	0.364	0.407	0.406	0.439	0.371	0.409	0.390	0.424	0.366	0.416	0.383	0.416	0.346	0.416
Crypto	96	0.174	0.143	0.179	0.143	0.187	0.147	0.176	0.139	0.183	0.144	0.181	0.143	0.183	0.144	0.177	0.141	0.183	0.155
	192	0.182	0.149	0.188	0.154	0.191	0.153	0.186	0.151	0.189	0.155	0.191	0.153	0.190	0.155	0.188	0.152	0.195	0.169
	336	0.191	0.158	0.197	0.166	0.197	0.163	0.192	0.162	0.201	0.168	0.208	0.173	0.199	0.167	0.195	0.164	0.206	0.180
	720	0.201	0.179	0.207	0.186	0.216	0.190	0.205	0.184	0.210	0.187	0.215	0.189	0.212	0.189	0.208	0.185	0.219	0.201
	AVG	0.187	0.157	0.193	0.162	0.198	0.163	0.190	0.159	0.196	0.164	0.199	0.165	0.196	0.164	0.192	0.161	0.201	0.176
Weather	96	0.159	0.206	0.175	0.215	0.165	0.208	0.175	0.217	0.203	0.244	0.158	0.203	0.175	0.216	0.176	0.217	0.197	0.259
	192	0.212	0.249	0.223	0.257	0.215	0.254	0.219	0.256	0.247	0.277	0.211	0.252	0.225	0.257	0.223	0.257	0.238	0.299
	336	0.265	0.288	0.278	0.297	0.273	0.297	0.275	0.298	0.297	0.311	0.267	0.292	0.280	0.298	0.277	0.296	0.282	0.331
	720	0.347	0.340	0.355	0.349	0.354	0.349	0.353	0.349	0.368	0.356	0.351	0.346	0.358	0.350	0.354	0.348	0.350	0.388
	AVG	0.246	0.271	0.258	0.280	0.252	0.277	0.256	0.280	0.279	0.279	0.247	0.273	0.260	0.280	0.258	0.280	0.267	0.319
1 st /2 nd Count		33	31	3	3	0	1	11	10	2	2	9	9	1	1	10	13	2	1